

# Coordination Chemistry of Bifunctional Chemical Agents Designed for Applications in $^{64}\text{Cu}$ PET Imaging for Alzheimer's Disease

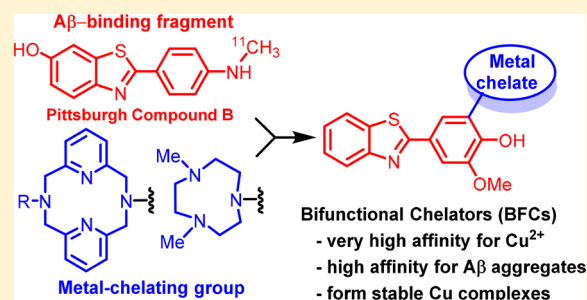
Anuj K. Sharma,<sup>†,‡</sup> Jason W. Schultz,<sup>†</sup> John T. Prior,<sup>†</sup> Nigam P. Rath,<sup>§</sup> and Liviu M. Mirica<sup>\*,†</sup>

<sup>†</sup>Department of Chemistry, Washington University, One Brookings Drive, St. Louis, Missouri 63130-4899, United States

<sup>§</sup>Department of Chemistry and Biochemistry, University of Missouri St. Louis, One University Boulevard, St. Louis, Missouri 63121-4400, United States

## Supporting Information

**ABSTRACT:** Positron emission tomography (PET) is emerging as one of the most important diagnostic tools for brain imaging, yet the most commonly used radioisotopes in PET imaging,  $^{11}\text{C}$  and  $^{18}\text{F}$ , have short half-lives, and their usage is thus somewhat limited. By comparison, the  $^{64}\text{Cu}$  radionuclide has a half-life of 12.7 h, which is ideal for administering and imaging purposes. In spite of appreciable research efforts, high-affinity copper chelators suitable for brain imaging applications are still lacking. Herein, we present the synthesis and characterization of a series of bifunctional compounds (BFCs) based on macrocyclic 1,4,7-triazacyclononane and 2,11-diaza[3.3]-(2,6)pyridinophane ligand frameworks that exhibit a high affinity for  $\text{Cu}^{2+}$  ions. In addition, these BFCs contain a 2-phenylbenzothiazole fragment that is known to interact tightly with amyloid  $\beta$  fibrillar aggregates. Determination of the protonation constants ( $\text{pK}_a$  values) and stability constants ( $\log \beta$  values) of these BFCs, as well as characterization of the isolated copper complexes using X-ray crystallography, electron paramagnetic resonance spectroscopy, and electrochemical studies, suggests that these BFCs exhibit desirable properties for the development of novel  $^{64}\text{Cu}$  PET imaging agents for Alzheimer's disease.



## INTRODUCTION

Alzheimer's disease (AD) is the most common neurodegenerative disease and the sixth leading cause of death in the United States.<sup>1,2</sup> Around 5 million people are presently diagnosed with AD in the U.S.<sup>3</sup> The brains of AD patients are characterized by the deposition of amyloid plaques containing the amyloid  $\beta$  ( $\text{A}\beta$ ) peptide.<sup>4–7</sup> To date, there is no treatment for AD,<sup>8</sup> and its diagnosis with high accuracy requires a detailed postmortem examination of the brain.<sup>2</sup> Thus, the effective imaging of various  $\text{A}\beta$  aggregates leads to an early diagnosis of AD.

Positron emission tomography (PET) is emerging as one of the most important diagnostic tools for brain imaging.<sup>9–11</sup> Recently,  $^{11}\text{C}$ - and  $^{18}\text{F}$ -radiolabeled agents, such as [ $^{11}\text{C}$ ]-PIB,<sup>11,12</sup> [ $^{11}\text{C}$ ]-SB-13,<sup>13</sup> [ $^{18}\text{F}$ ]-BAY94-9172,<sup>14</sup> [ $^{11}\text{C}$ ]-BF-227,<sup>15</sup> [ $^{18}\text{F}$ ]-FDDNP,<sup>16</sup> and [ $^{18}\text{F}$ ]-AV-45,<sup>17,18</sup> have been developed for noninvasive PET imaging of mature amyloid plaques in AD patients (Figure 2b).<sup>12,19–26</sup> However, these agents are limited by their short physical half-life ( $t_{1/2} = 20.4$  and 109.8 min, respectively) and their complex synthesis. By comparison, the  $^{64}\text{Cu}$  radionuclide can be viewed as an ideal positron emitter for PET imaging because of its decay scheme ( $\beta^+$ , 19%;  $\beta^-$ , 40%; electron capture, 40%) and an optimal half-life of 12.7 h.<sup>27–29</sup>

The development of chelators that form copper complexes stable enough to withstand transmetalation in vivo remains a challenge.<sup>28</sup> For example, the commonly studied 1,4,7,10-tetraazacyclododecane- $N,N',N'',N'''$ -tetraacetic acid and

2,2',2'',2'''-(1,4,8,11-tetraazacyclotetradecane-1,4,8,11-tetrayl)-tetraacetic acid ligands were shown to form stable complexes of copper(2+) with high thermodynamic stability but presented limited kinetic inertness to avoid demetalation.<sup>28,30</sup> In order to get more kinetically inert complexes, cage-like polyaza chelators, such as bicyclic hexaamines, dicarboxylic acid cross-bridged cyclen, and cyclam, were subsequently developed.<sup>31–47</sup> However, these latter systems suffer from low rates of metalation, which require high temperatures and thus limit the development of bioconjugated imaging agents. Recently, multidentate ligands based on cyclen, 1,4,7-triazacyclononane (tacn), and bispidine macrocycles were shown to rapidly form copper complexes with remarkable inertness.<sup>48–50</sup>

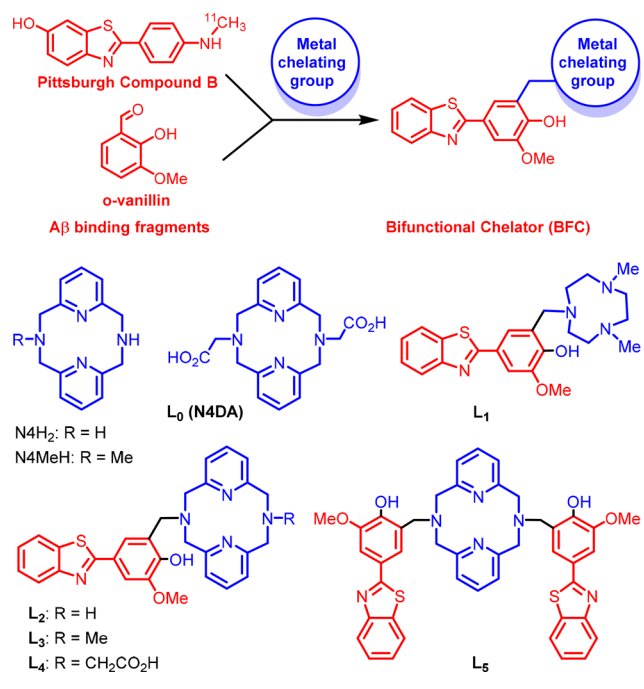
We have recently reported the development of bifunctional chelators (BFCs), which can bind metal ions and also interact with  $\text{A}\beta$  aggregates and thus modulate the aggregation and neurotoxicity of various  $\text{A}\beta$  species.<sup>51–54</sup> Moreover, we envisioned that the BFCs that exhibit a very high affinity for Cu ions could be used to prechelate  $^{64}\text{Cu}$  and thus generate PET imaging agents that also have an affinity for  $\text{A}\beta$  aggregates. On the basis of this strategy, described herein are BFCs that contain tacn or 2,11-diaza[3.3](2,6)pyridinophane (N4) macrocycles as the metal chelating fragments along with a  $\text{A}\beta$ -binding 2-phenylbenzothiazole moiety, reminiscent of ThT

Received: July 23, 2017

Published: November 7, 2017

and PiB (Scheme 1).<sup>11,12,55</sup> Both tacn and N4 macrocycles have been shown previously to act as high-affinity metal

### Scheme 1. Design Strategy and Structures of Various Ligands Developed Herein



chelators.<sup>37,56,57</sup> The synthesis and characterization of the copper complexes of ligands L<sub>0</sub>–L<sub>5</sub>, along with their stability constant determination, X-ray structural characterization, electron paramagnetic resonance, and electrochemical studies, are reported herein. On the basis of the obtained results, the developed bifunctional chelating agents show promise to be used in <sup>64</sup>Cu-radiolabeling and PET imaging studies.

## EXPERIMENTAL SECTION

**General Methods.** All reagents were purchased from commercial sources and used as received unless stated otherwise. Solvents were purified prior to use by passing through a column of activated alumina using an MBraun SPS. The precursors 2,11-diaza[3.3](2,6)-pyridinophane (N4H<sub>2</sub>),<sup>58</sup> N-methyl-2,11-diaza[3.3](2,6)-pyridinophane (N4MeH),<sup>59</sup> and 1,4-dimethyl-1,4,7-triazacyclononane<sup>60</sup> were prepared following literature protocols. All solutions and buffers were prepared using metal-free Millipore water (H<sub>2</sub>O) that was treated with Chelex overnight and filtered through a 0.22  $\mu$ m nylon filter. <sup>1</sup>H (300.121 MHz) and <sup>13</sup>C (75 MHz) NMR spectra were recorded on a Varian Mercury-300 spectrometer. Chemical shifts are reported in parts per million and referenced to residual solvent resonance peaks. UV–vis spectra were recorded on a Varian Cary 50 Bio spectrophotometer and are reported as  $\lambda_{\text{max}}$ , nm ( $\epsilon$ , M<sup>-1</sup> cm<sup>-1</sup>). Electrospray ionization mass spectrometry (ESI-MS) experiments were performed at the Washington University Mass Spectrometry NIH Resource (Grant P41RR0954) using a Bruker Maxis Q-TOF mass spectrometer with an electrospray ionization source. Elemental analyses were performed by the Columbia Analytical Services Tucson Laboratory. Transmission electron microscopy (TEM) analysis was performed at the Nano Research Facility (NRF) at Washington University (St. Louis, MO). All fluorescence measurements were performed using a SpectraMax M2e plate reader (Molecular Devices). Electron paramagnetic resonance (EPR) spectra were recorded on a JEOL JES-FA X-band (9.2 GHz) EPR spectrometer at 77 K.

**Synthesis of BFCs.** L<sub>0</sub> (N4DA). N4H<sub>2</sub> (250 mg) was suspended in 15 mL of dry acetonitrile (MeCN) along with sodium carbonate

(0.220 g, 2.2 equiv) and *tert*-butyl bromoacetate (307.2  $\mu$ L, 2.0 equiv), and the suspension was stirred under reflux for 14 h. The solution was then cooled and filtered, and the filtrate was concentrated to dryness under vacuum to give a pale-yellow powder of N4(CH<sub>2</sub>COO<sup>t</sup>Bu)<sub>2</sub> (0.494 g, 96.5%). <sup>1</sup>H NMR (300 MHz, CDCl<sub>3</sub>):  $\delta$  7.10 (t, 2H, arom-H), 6.55 (d, 4H, arom-H), 4.26 (d, 4H, –CH<sub>2</sub>–), 3.76 (s, 4H, –CH<sub>2</sub>–), 3.65 (d, 4H, –CH<sub>2</sub>–), 1.54 (s, 18H, –CH<sub>3</sub>). The ester was dissolved in 20 mL of 5 M HCl and refluxed with stirring for 12 h. The solvent was removed to get an off-white powder, which was dissolved in absolute ethanol and filtered. Removal of the solvent gave a white powder, which was dried under vacuum to obtain the product as L<sub>0</sub>·4HCl (0.510 g, yield 96%). <sup>1</sup>H NMR (300 MHz, D<sub>2</sub>O):  $\delta$  7.70 (t, 2H, arom-H), 7.18 (d, 4H, arom-H), 4.49 (s, 8H, –CH<sub>2</sub>–Py), 4.19 (s, 4H, –CH<sub>2</sub>–COOH). ESI-MS. Calcd for [M + H]<sup>+</sup>: *m/z* 357.2. Found: *m/z* 357.2.

L<sub>1</sub>.<sup>61</sup> Paraformaldehyde (0.204 g, 6.68 mmol) was added to a solution of 1,4-dimethyl-1,4,7-triazacyclononane (0.7 g, 4.45 mmol) in MeCN (5 mL), and the resultant mixture was heated to reflux for 30 min. Then 2-(4-hydroxy-3-methoxy)benzothiazole (1.145 g, 4.45 mmol) in MeCN (35 mL) was added, and the solution was refluxed for 24 h under N<sub>2</sub>. Upon cooling to room temperature, the solvent was removed to give a reddish residue, which was purified by silica gel column chromatography using CHCl<sub>3</sub>/methanol (MeOH)/NH<sub>4</sub>OH (90:5:5) to yield a yellow oil (0.55 g, yield 30%). <sup>1</sup>H NMR (CDCl<sub>3</sub>):  $\delta$  8.01 (d, 1H, ArH), 7.86 (d, 1H, ArH), 7.54 (s, 1H, ArH), 7.45 (t, 1H, ArH), 7.35–7.31 (m, 2H, ArH), 4.10 (s, 3H, OCH<sub>3</sub>), 3.93 (s, 2H, NCH<sub>2</sub>Py), 3.01 (t, 4H, CH<sub>2</sub>N), 2.72 (t, 4H, CH<sub>2</sub>N), 2.56 (s, 4H, CH<sub>2</sub>N), 2.39 (s, 6H, NCH<sub>3</sub>). <sup>13</sup>C NMR (CDCl<sub>3</sub>):  $\delta$  168.52, 154.19, 151.58, 148.52, 134.70, 126.12, 124.57, 123.81, 122.92, 122.56, 121.42, 120.62, 109.61, 60.52, 58.55, 57.99, 56.11, 53.14, 46.72. UV–vis [MeCN;  $\lambda_{\text{max}}$  nm ( $\epsilon$ , M<sup>-1</sup> cm<sup>-1</sup>): 330 (18200). ESI-MS. Calcd for [M + H]<sup>+</sup>: *m/z* 427.1. Found: *m/z* 427.1.

L<sub>2</sub> and L<sub>5</sub>.<sup>61</sup> Paraformaldehyde (0.062 g, 2.08 mmol) was added to a solution of N<sub>4</sub>H<sub>2</sub> (0.050 g, 0.208 mmol) in MeCN (2 mL), and the resultant mixture was heated to reflux for 1 h. A hot solution of 2-(4-hydroxy-3-methoxy)benzothiazole (0.054 g, 0.208 mmol) in MeCN (5 mL) was added to the reaction flask, and the solution was refluxed for another 24 h under N<sub>2</sub>. The solvent was removed, and the resulting residue was purified by silica gel column chromatography using ethyl acetate (EtOAc) to elute the unreacted 2-(4-hydroxy-3-methoxy)benzothiazole, followed by 90:10 CHCl<sub>3</sub>/MeOH to elute the dibenzothiazole product L<sub>5</sub> and then by 80:20 CHCl<sub>3</sub>/MeOH to elute L<sub>2</sub>. The solvent was removed to yield L<sub>2</sub> as a yellow solid (0.062 g, yield 60%). **Characterization of L<sub>2</sub>.** <sup>1</sup>H NMR (CDCl<sub>3</sub>):  $\delta$  8.03 (d, 1H, ArH), 7.88 (d, 1H, ArH), 7.64 (s, 1H, ArH), 7.53 (s, 1H, ArH), 7.45 (t, 1H, ArH), 7.35 (t, 1H, ArH), 7.12 (t, 2H, PyH), 6.73 (d, 2H, PyH), 6.54 (d, 2H, PyH), 4.29 (s, 2H, NCH<sub>2</sub>–), 4.07 (s, 4H, CH<sub>2</sub>NCH<sub>2</sub>), 4.06 (s, 3H, OCH<sub>3</sub>), 4.07 (s, 4H, CH<sub>2</sub>NCH<sub>2</sub>). <sup>13</sup>C NMR (CDCl<sub>3</sub>):  $\delta$  168.17, 156.52, 154.12, 136.51, 134.77, 126.24, 123.24, 122.69, 121.88, 121.53, 120.97, 110.70, 63.33, 56.37, 55.09. UV–vis [MeCN;  $\lambda_{\text{max}}$  nm ( $\epsilon$ , M<sup>-1</sup> cm<sup>-1</sup>): 334 (15800). ESI-MS. Calcd for [M + H]<sup>+</sup>: *m/z* 510.1964. Found: *m/z* 510.2.

**Characterization of L<sub>5</sub>.** Yield: 16%. <sup>1</sup>H NMR (CDCl<sub>3</sub>):  $\delta$  7.99 (d, 1H, ArH), 7.84 (d, 1H, ArH), 7.64 (s, 1H, ArH), 7.47 (s, 1H, ArH), 7.45 (t, 1H, ArH), 7.33 (t, 1H, ArH), 7.18 (t, 2H, PyH), 6.83 (d, 2H, PyH), 4.23 (s, 4H, NCH<sub>2</sub>–), 4.05 (s, br, 6H, –OCH<sub>3</sub>, and 8H, CH<sub>2</sub>NCH<sub>2</sub>). <sup>13</sup>C NMR (CDCl<sub>3</sub>):  $\delta$  168.04, 155.75, 154.10, 150.06, 148.79, 134.76, 126.26, 125.10, 124.82, 123.06, 122.71, 120.74, 110.24, 63.67, 56.24. UV–vis [MeCN;  $\lambda_{\text{max}}$  nm ( $\epsilon$ , M<sup>-1</sup> cm<sup>-1</sup>): 323 (19600). ESI-MS. Calcd for [M + H]<sup>+</sup>: *m/z* 779.2474. Found: *m/z* 779.3.

L<sub>3</sub>.<sup>61</sup> Paraformaldehyde (0.088 g, 2.95 mmol) was added to a solution of N4MeH (0.050 g, 0.196 mmol) in MeCN (5 mL), and the resultant mixture was heated to reflux for 1 h. A hot solution of 2-(4-hydroxy-3-methoxy)benzothiazole (0.076 g, 0.295 mmol) in MeCN (5 mL) was added to the reaction flask, and the solution was refluxed for another 24 h under N<sub>2</sub>. The solvent was removed, and the resulting residue was purified by silica gel column chromatography using EtOAc to elute out the remaining starting material 2-(4-hydroxy-3-methoxy)benzothiazole and then a 80:15:5 ratio of CHCl<sub>3</sub>/MeOH/NH<sub>4</sub>OH to elute out the product. The solvent was removed to yield a yellow solid

(0.045 g, yield 44%).  $^1\text{H NMR}$  ( $\text{CDCl}_3$ ):  $\delta$  8.02 (d, 1H, ArH), 7.86 (d, 1H, ArH), 7.63 (s, 1H, ArH), 7.48 (s, 1H, ArH), 7.45 (t, 1H, ArH), 7.33 (t, 1H, ArH), 7.14 (t, 2H, PyH), 6.80 (t, 4H, PyH), 4.24 (s, 2H,  $\text{NCH}_2$ ), 4.08 (s, 4H,  $\text{CH}_2\text{NCH}_2$ ), 4.05 (s, 3H,  $\text{OCH}_3$ ), 3.82 (s, 4H,  $\text{CH}_2\text{NHCH}_2$ ), 2.71 (s, 3H,  $\text{NCH}_3$ ).  $^{13}\text{C NMR}$  ( $\text{CDCl}_3$ ):  $\delta$  168.05, 154.11, 150.09, 148.74, 126.25, 125.06, 124.81, 123.066, 122.71, 122.61, 121.51, 120.76, 110.165, 65.91, 59.81, 56.22, 42.73. UV-vis [MeCN;  $\lambda_{\text{max}}$  nm ( $\epsilon$ ,  $\text{M}^{-1} \text{cm}^{-1}$ ): 330 (9740). ESI-MS. Calcd for  $[\text{M} + \text{H}]^+$ :  $m/z$  524.2645. Found:  $m/z$  524.2.

**L<sub>4</sub>.** To a solution of **L<sub>2</sub>** (0.045 g, 0.088 mmol) in MeCN (5 mL) was added  $\text{Na}_2\text{CO}_3$  (0.0093 g, 0.088 mmol), followed by the addition of *tert*-butyl bromoacetate (0.0172 g, 0.088 mmol), and the resultant mixture was stirred for 3 h at room temperature under  $\text{N}_2$ . Then solvent was removed, and the resulting residue was purified by silica gel column chromatography using 95:5  $\text{CHCl}_3/\text{MeOH}$  to elute out the product. The solvent was removed to yield a yellow solid (0.054 g, yield 98%). **Characterization of the ester precursor.**  $^1\text{H NMR}$  ( $\text{CDCl}_3$ ):  $\delta$  7.96 (d, 1H, ArH), 7.88 (d, 1H, ArH), 7.58–7.34 (m, 4H, ArH), 7.08 (t, 2H, ArH), 6.54–6.47 (m, 2H, ArH), 4.39–4.21 (m, 8H,  $\text{NCH}_2$ ), 4.07 (s, 3H,  $\text{OCH}_3$ ), 3.97–3.90 (s, 2H,  $\text{CH}_2\text{NCH}_2$ ), 3.58 (s, 2H,  $\text{CH}_2\text{NHCH}_2$ ), 1.49 (s, 9H, tBu). HRMS. Calcd for  $[\text{M} + \text{H}]^+$ :  $m/z$  624.2645. Found:  $m/z$  624.3. The ester intermediate was dissolved in 6 M HCl and stirred for 12 h at room temperature. The solvent was removed under vacuum to yield a yellow solid.  $^1\text{H NMR}$  ( $\text{CD}_3\text{OD}$ ):  $\delta$  8.24 (s, 1H, ArH), 8.11–8.03 (m, 2H, ArH), 7.89 (s, 1H, ArH), 7.67–7.51 (m, 4H, ArH), 7.20–7.12 (m, 4H, ArH), 5.07 (s, 2H,  $\text{NCH}_2$ ), 4.90 (m, 8H,  $\text{NCH}_2$ ), 4.71 (s, 2H,  $\text{NCH}_2$ ), 4.09 (s, 3H,  $\text{OCH}_3$ ).  $^{13}\text{C NMR}$  ( $\text{CD}_3\text{OD}$ ):  $\delta$  190.57, 166.98, 154.24, 149.71, 149.43, 148.93, 138.81, 132.43, 131.15, 128.54, 127.01, 126.44, 123.57, 123.44, 119.69, 118.57, 111.56, 60.68, 59.47, 56.07, 55.80, 53.16. UV-vis [MeCN;  $\lambda_{\text{max}}$  nm ( $\epsilon$ ,  $\text{M}^{-1} \text{cm}^{-1}$ ): 331 (12300). ESI-MS. Calcd for  $[\text{M} + \text{H}]^+$ :  $m/z$  568.2019. Found:  $m/z$  568.2.

**Syntheses of Metal Complexes.**  $[(\text{L}_0)_4\text{Cu}^{\text{II}}](\text{ClO}_4)_4$  (**1**) and  $[(\text{L}_0)\text{Cu}^{\text{II}}\text{Cl}_2]$  (**2**). To an aqueous solution of  $\text{L}_0$ -4HCl (0.050 g, 0.1 mmol) was added an aqueous solution of  $\text{Cu}(\text{ClO}_4)_2 \cdot 6\text{H}_2\text{O}$  (37 mg, 0.1 mmol), and the pH of the green reaction mixture was adjusted to 5.5 with a 1 M NaOH solution. After stirring for 2 h at room temperature, the solvent was removed to obtain a light-green residue. Recrystallization in hot MeCN provided crystals of **1**. This complex was further dissolved in 1 M HCl, and slow evaporation yielded single crystals of **2** (0.058 g, yield 58%). UV-vis [MeOH/ $\text{H}_2\text{O}$ ;  $\lambda_{\text{max}}$  nm ( $\epsilon$ ,  $\text{M}^{-1} \text{cm}^{-1}$ ): 810 (95). Anal. Calcd for  $\text{C}_{18}\text{H}_{20}\text{Cl}_2\text{N}_4\text{O}_4\text{Cu} \cdot 2.5\text{H}_2\text{O}$  (**2**): C, 40.34; H, 4.70; N, 10.46. Found: C, 40.17; H, 4.43; N, 10.27.

$[(\text{L}_1)\text{Cu}^{\text{II}}\text{Cl}]$  (**3**).<sup>61</sup> To a stirring solution of **L<sub>1</sub>** (0.125 g, 0.293 mmol) in MeCN (5 mL) and triethylamine ( $\text{Et}_3\text{N}$ ; 0.044 g, 0.44 mmol) was added a solution of  $\text{CuCl}_2$  (0.040 g, 0.293 mmol) in MeCN (2 mL). The brown solution was stirred for 30 min. The addition of diethyl ether ( $\text{Et}_2\text{O}$ ) resulted in the formation of a brown precipitate, which was filtered and washed with  $\text{Et}_2\text{O}$  and dried under vacuum (0.085 g, yield 55%). UV-vis [MeCN;  $\lambda_{\text{max}}$  nm ( $\epsilon$ ,  $\text{M}^{-1} \text{cm}^{-1}$ ): 353 (7500), 425 (sh, 450), 515 (sh, 250), 650 (90). ESI-MS. Calcd for  $[(\text{L}_1)\text{Cu}]^+$ :  $m/z$  488.1307. Found:  $m/z$  488.1. Anal. Calcd for  $\text{C}_{23}\text{H}_{29}\text{ClN}_4\text{O}_2\text{SCu} \cdot 2\text{H}_2\text{O}$ : C, 48.50; H, 6.02; N, 9.84. Found: C, 48.42; H, 6.69; N, 9.47.

$[(\text{L}_1)\text{Zn}^{\text{II}}(\text{MeCN})_2](\text{ClO}_4)_4$  (**4**). A solution of  $\text{Zn}(\text{ClO}_4)_2 \cdot 6\text{H}_2\text{O}$  (0.044 g, 0.117 mmol) was added to a stirring solution of **L<sub>1</sub>** (0.050 g, 0.117 mmol) in MeCN (5 mL) and  $\text{Et}_3\text{N}$  (0.012 g, 0.117 mmol). The resulting solution was stirred for 4 h. The addition of  $\text{Et}_2\text{O}$  (20 mL) resulted in the formation of a white precipitate, which was filtered, washed with  $\text{Et}_2\text{O}$ , and dried under vacuum (0.028 g, yield 36%). ESI-MS. Calcd for  $[(\text{L}_1)\text{Zn}]^+$ :  $m/z$  489.1. Found:  $m/z$  489.1. Anal. Calcd for  $\text{C}_{27}\text{H}_{35}\text{ClZnN}_6\text{O}_8\text{S} \cdot \text{H}_2\text{O}$ : C, 46.96; H, 5.40; N, 12.17. Found: C, 46.65; H, 5.61; N, 12.06.

$[(\text{L}_2)_2\text{Cu}^{\text{II}}](\text{ClO}_4)_2$  (**5**).<sup>61</sup> A solution of  $\text{Cu}(\text{ClO}_4)_2 \cdot 6\text{H}_2\text{O}$  (0.036 g, 0.098 mmol) was added to a stirring solution of **L<sub>2</sub>** (0.050 g, 0.098 mmol) in MeOH (5 mL) and  $\text{Et}_3\text{N}$  (0.015 g, 0.147 mmol). The brown solution was stirred for 12 h. A reddish-brown precipitate was formed, which was filtered, washed with  $\text{Et}_2\text{O}$ , and dried under vacuum (0.052 g, yield 79%). UV-vis [MeCN;  $\lambda_{\text{max}}$  nm ( $\epsilon$ ,  $\text{M}^{-1} \text{cm}^{-1}$ ): 363 (15000), 428 (1500), 505 (450), 725 (130). ESI-MS. Calcd for  $[(\text{L}_2)\text{Cu}]^+$ :  $m/z$

571.1. Found:  $m/z$  571.1. Anal. Calcd for  $\text{C}_{58}\text{H}_{52}\text{Cl}_2\text{N}_{10}\text{O}_4\text{S}_2\text{Cu}_2$ : C, 51.86; H, 3.90; N, 10.43. Found: C, 51.15; H, 3.86; N, 10.20.

$[(\text{L}_3)\text{Cu}^{\text{II}}](\text{ClO}_4)_4$  (**6**). A solution of  $\text{Cu}(\text{ClO}_4)_2 \cdot 6\text{H}_2\text{O}$  (0.042 g, 0.114 mmol) was added to a stirring solution of **L<sub>3</sub>** (0.060 g, 0.114 mmol) in MeOH (5 mL) and  $\text{Et}_3\text{N}$  (0.018 g, 0.171 mmol). The brown solution was stirred for 12 h. The addition of  $\text{Et}_2\text{O}$  (30 mL) resulted in the formation of a brown precipitate, which was filtered, washed with  $\text{Et}_2\text{O}$ , and dried under vacuum (0.052 g, yield 79%). UV-vis [MeCN;  $\lambda_{\text{max}}$  nm ( $\epsilon$ ,  $\text{M}^{-1} \text{cm}^{-1}$ ): 357 (14700), 421 (1600), 520 (430), 710 (150). ESI-MS. Calcd for  $[(\text{L}_3)\text{Cu}]^+$ :  $m/z$  585.1. Found:  $m/z$  585.1. Anal. Calcd for  $\text{C}_{30}\text{H}_{34}\text{ClN}_5\text{O}_5\text{SCu}$ : C, 48.71; H, 4.63; N, 9.47. Found: C, 48.43; H, 4.10; N, 9.38.

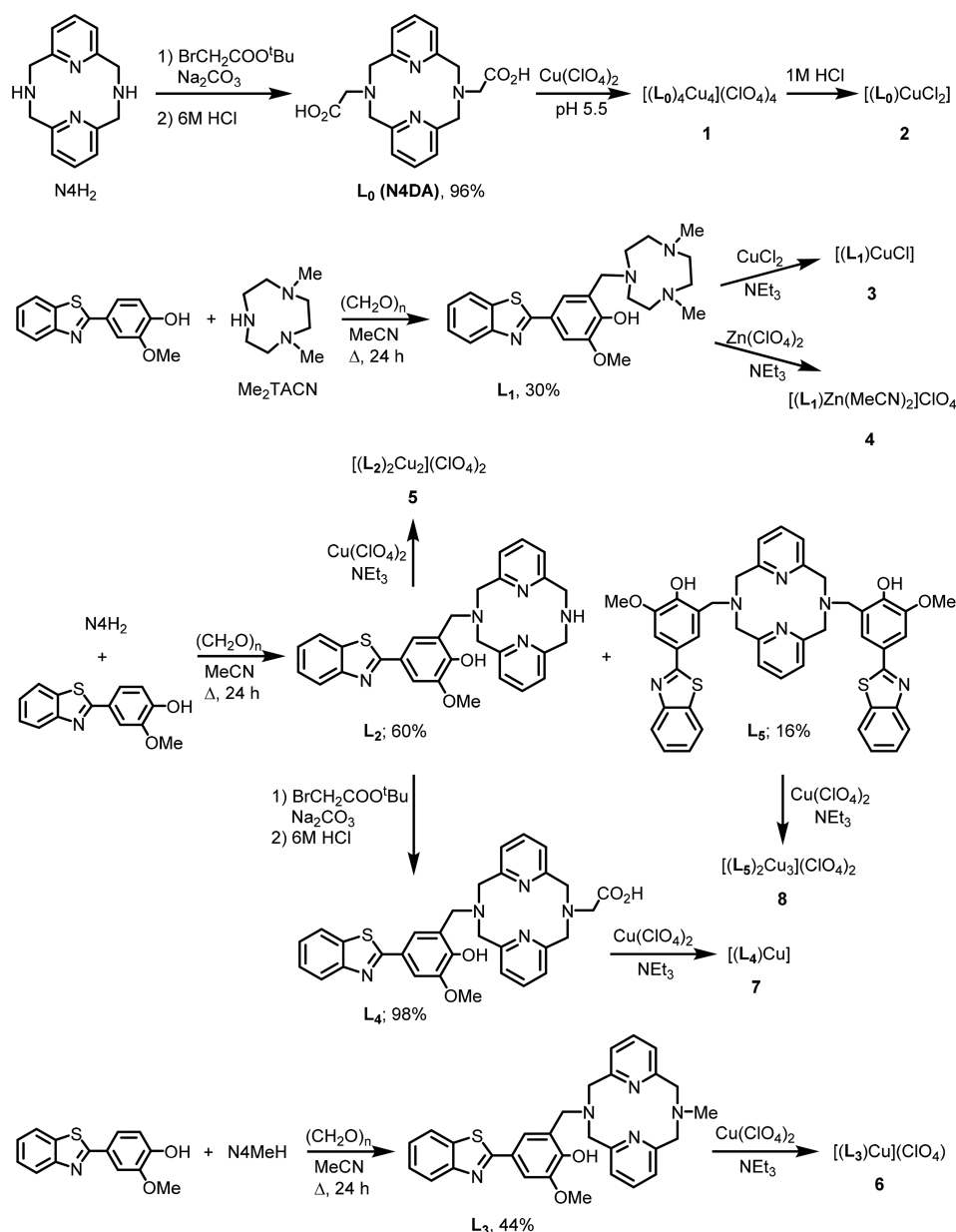
$[(\text{L}_4)\text{Cu}^{\text{II}}]$  (**7**).<sup>61</sup> A solution of  $\text{Cu}(\text{ClO}_4)_2 \cdot 6\text{H}_2\text{O}$  (0.032 g, 0.088 mmol) was added to a stirring solution of **L<sub>4</sub>** (0.050 g, 0.088 mmol) in MeOH (5 mL), which formed a green solution. The drop-by-drop addition of  $\text{Et}_3\text{N}$  (0.045 g, 0.44 mmol) resulted in a deep-brown solution, which was stirred for 12 h. The addition of  $\text{Et}_2\text{O}$  (20 mL) resulted in the formation of a brown precipitate, which was filtered, washed with  $\text{Et}_2\text{O}$ , and dried under vacuum (0.042 g, yield 65%). UV-vis [MeCN;  $\lambda_{\text{max}}$  nm ( $\epsilon$ ,  $\text{M}^{-1} \text{cm}^{-1}$ ): 358 (12000), 425 (1300), 500 (430), 761 (120). HRMS. Calcd for  $[(\text{L}_4)\text{Cu}]^+$ :  $m/z$  629.1. Found:  $m/z$  629.1. Anal. Calcd for  $\text{C}_{32}\text{H}_{31}\text{ClN}_5\text{O}_5\text{SCu} \cdot 2\text{H}_2\text{O}$ : C, 49.23; H, 4.52; N, 8.97. Found: C, 49.12; H, 4.22; N, 8.63.

$[(\text{L}_5)_2\text{Cu}^{\text{II}}]$  (**8**).<sup>61</sup> A solution of  $\text{Cu}(\text{ClO}_4)_2 \cdot 6\text{H}_2\text{O}$  (0.056 g, 0.088 mmol) was added to a stirring solution of **L<sub>5</sub>** (0.118 g, 0.151 mmol) in MeOH (5 mL). The deep-brown solution was stirred for 12 h. The addition of  $\text{Et}_2\text{O}$  (30 mL) resulted in the formation of a brown precipitate, which was filtered, washed with  $\text{Et}_2\text{O}$ , and dried under vacuum (0.101 g, yield 79%). UV-vis [MeCN;  $\lambda_{\text{max}}$  nm ( $\epsilon$ ,  $\text{M}^{-1} \text{cm}^{-1}$ ): 324 (14000), 410 (4500), 560 (1400), 750 (sh, 180). ESI-MS. Calcd for  $[(\text{L}_5)_2\text{Cu}]^+$ :  $m/z$  840.1614. Found:  $m/z$  840.2. Anal. Calcd for  $\text{C}_{88}\text{H}_{74}\text{Cl}_2\text{Cu}_3\text{N}_{12}\text{O}_{17}\text{S}_4 \cdot 4\text{H}_2\text{O} \cdot 2\text{MeOH}$ : C, 51.53; H, 4.33; N, 8.01. Found: C, 51.04; H, 3.50; N, 8.00.

**Caution!** Perchlorate salts of compounds containing organic ligands are potentially explosive, and hence only the synthesis of small amounts of the complexes should be attempted.

**X-ray Crystallography.** Suitable crystals of appropriate dimensions were mounted on a Bruker Apex II CCD X-ray diffractometer equipped with an Oxford Cryostream LT device and a fine-focus Mo  $K\alpha$  radiation X-ray source ( $\lambda = 0.71073 \text{ \AA}$ ). Preliminary unit cell constants were determined with a set of 36 narrow frame scans. Typical data sets consist of a combinations of  $\omega$  and  $\phi$  scan frames with a typical scan width of  $0.5^\circ$  and a counting time of 15–30 s frame<sup>-1</sup> at a crystal-to-detector distance of  $\sim 4.0 \text{ cm}$ . The collected frames were integrated using an orientation matrix determined from the narrow-frame scans. *Apex II* and *SAINTE* software packages (Bruker Analytical X-ray, Madison, WI) were used for data collection and data integration. The final cell constants were determined by the global refinement of reflections from the complete data set. Data were corrected for systematic errors using *SADABS* (Bruker Analytical X-ray, Madison, WI). Structure solutions and refinement were carried out using the *SHELXTL-PLUS* software package.<sup>62</sup> The structures were refined with full-matrix least-squares refinement by minimizing  $\sum w(F_o^2 - F_c^2)^2$ . All non-H atoms were refined anisotropically to convergence. All H atoms were added in the calculated position and refined using appropriate riding models (AFIX  $m^3$ ). Additional crystallographic details can be found in the [Supporting Information](#).<sup>63</sup>

**Acidity and Stability Constant Determination.** UV-vis pH titrations were employed for determination of the acidity constants of **L<sub>0</sub>**–**L<sub>5</sub>** and the stability constants of their copper(2+) complexes. For the acidity constants, solutions of BFCs (50  $\mu\text{M}$ , 0.1 M NaCl, pH 3) were titrated with small aliquots of 0.1 M NaOH at room temperature. About 30 UV-vis spectra were collected in the pH 3–11 range. Because of the limited solubility of **L<sub>1</sub>**–**L<sub>5</sub>** in  $\text{H}_2\text{O}$ , MeOH stock solutions (10 mM) were used and titrations were performed in a MeOH/ $\text{H}_2\text{O}$  mixture in which MeOH did not exceed 20% (v/v) and the pH range could not be extended beyond 3 and 11. Similarly, the stability constants were determined by titrating solutions of **L<sub>0</sub>**–**L<sub>5</sub>** and equimolar amounts of  $\text{Cu}(\text{ClO}_4)_2 \cdot 6\text{H}_2\text{O}$  (50  $\mu\text{M}$  or 0.5 mM) with small aliquots of 0.1 M NaOH at room temperature. About 30 UV-vis

Scheme 2. Syntheses of Ligands L<sub>0</sub>–L<sub>5</sub> and the Corresponding Metal Complexes

spectra were collected in the pH 3–11 range. The acidity and stability constants were calculated using the *HypSpec* computer program (Protonic Software, UK).<sup>64</sup> Speciation plots of the compounds and their metal complexes were calculated using the program *HySS2009* (Protonic Software, UK).<sup>65</sup>

**Electrochemical Studies.** Cyclic voltammograms were performed in aqueous solution at room temperature with a BASi EC Epsilon electrochemical workstation or CHI 660D electrochemical analyzer. The three-electrode setup consisted of a reference Ag/AgCl electrode, a platinum wire auxiliary electrode, and a glassy carbon working electrode. A solution of the copper(2+) complexes of BFCs in MeCN at 2 mM concentration was mixed with an equal volume of H<sub>2</sub>O (0.2 M CH<sub>3</sub>COONa electrolyte). The electrochemical measurements were performed under a blanket of N<sub>2</sub>. Analyzed solutions were deaerated by purging with N<sub>2</sub>. Between each scan, the working electrode was cleaned by polishing on alumina, cleaned with H<sub>2</sub>O and MeOH. Cyclic voltammograms with sweep rates ranging from 100 to 1000 mV s<sup>-1</sup> were recorded in the range of +1200 to -1200 mV. At this potential range, the solvent mixture 1:1 MeCN/H<sub>2</sub>O was found to be electroinactive. The half-wave potentials, E<sub>1/2</sub>, were obtained by

averaging the anodic and cathodic peak potentials. All potential values are reported relative to the Ag/AgCl reference electrode in aqueous 3 M NaCl unless otherwise noted.

**Aβ Peptide Experiments.** Aβ monomeric films were prepared by dissolving commercial Aβ<sub>42</sub> (or Aβ<sub>40</sub> for the Aβ fibril binding studies) peptide (Keck Biotechnology Resource Laboratory, Yale University) in hexafluoro-2-propanol (1 mM) and incubating for 1 h at room temperature. The solution was then aliquoted out and evaporated overnight. The aliquots were vacuum-centrifuged and the resulting monomeric films stored at -80 °C. Aβ fibrils were generated by dissolving monomeric Aβ films in dimethyl sulfoxide (DMSO), diluting into the appropriate buffer, and incubating for 24 h at 37 °C with continuous agitation (the final DMSO concentration was <2%). For inhibition studies, BFCs (50 μM, DMSO stock solutions) were added to Aβ solutions (25 μM) in the absence or presence of metal salts (CuCl<sub>2</sub> or ZnCl<sub>2</sub>, 25 μM) and incubated for 24 h at 37 °C with constant agitation.

**Native Gel Electrophoresis and Western Blotting.** All gels, buffers, membranes, and other reagents were purchased from Invitrogen and used as directed, except where otherwise noted.

Samples were separated on 10–20% gradient Tris-tricine mini gels. The gel was transferred to a nitrocellulose membrane in an ice bath, and the protocol was followed as suggested, except that the membrane was blocked overnight at 4 °C. After blocking, the membrane was incubated in a solution (1:2000 dilution) of 6E10 anti-A $\beta$  primary antibody (Covance) for 3 h. Invitrogen's Western Breeze Chemiluminescent kit was used to visualize the bands. An alkaline phosphatase antimouse secondary antibody was used, and the protein bands were imaged using a Fujifilm LAS-1000CH luminescent image analyzer.

**TEM.** Glow-discharged grids (Formar/Carbon 300-mesh, Electron Microscopy Sciences) were treated with A $\beta$  samples (25  $\mu$ M, 5  $\mu$ L) for 2–3 min at room temperature. Excess solution was removed using filter paper, and the grids were rinsed twice with H<sub>2</sub>O (5  $\mu$ L). Then the grids were stained with uranyl acetate [1% (w/v) in H<sub>2</sub>O, 5  $\mu$ L] for 1 min, blotted with filter paper, and dried for 15 min at room temperature. Images were captured using a FEI G2 Spirit Twin microscope (60–80 kV, 6500–97000 $\times$  magnification). TEM analysis was performed at the NRF at Washington University.

## RESULTS

**Design, Synthesis, and General Properties of Compounds L<sub>0</sub>–L<sub>5</sub>.** The synthesis of compound N4DA (Scheme 2) was previously described by Sherry et al.<sup>56,57</sup> We used a slightly different procedure for its synthesis: the reaction of *tert*-butyl bromoacetate with N4H<sub>2</sub> forms a diester intermediate, which upon hydrolysis generates L<sub>0</sub> (N4DA) in quantitative yield. The BFCs L<sub>1</sub>–L<sub>5</sub> were synthesized via Mannich reactions between 2-(4-hydroxy-3-methoxyphenyl)benzothiazole and metal-chelating groups such as 2,4-dimethyl-1,4,7-triazacyclononane (Me<sub>2</sub>tacn) and N4H<sub>2</sub> or N4MeH in the presence of paraformaldehyde (Scheme 2). For the synthesis of L<sub>4</sub>, an acetate arm was introduced in L<sub>2</sub> by reaction with *tert*-butyl bromoacetate in MeCN, followed by ester hydrolysis in 6 M HCl (Scheme 2).

All synthesized compounds were characterized by <sup>1</sup>H and <sup>13</sup>C NMR, UV–vis and fluorescence spectroscopy, and ESI-MS. All BFCs exhibit absorption maxima at  $\sim$ 330 nm, and upon excitation at this wavelength, emission maxima are observed at  $\sim$ 450 nm (Figure 1). The BFCs L<sub>2</sub> and L<sub>3</sub> exhibit the highest intensities of emission, and the rest of the BFCs exhibit about the same fluorescence intensities, except L<sub>5</sub>, which shows the poorest emission spectra of all, most likely because of intermolecular quenching (Figure 1).

**Acidity Constant Determination.** Protonation constants for all of the compounds used in this study were determined from pH-spectrophotometric titrations.<sup>66</sup> Because ligands L<sub>0</sub>–L<sub>5</sub> have functional groups that can undergo protonation/deprotonation such as amine, pyridyl, and phenol groups, multiple protonation constants (pK<sub>a</sub>) are expected. Two protonation constants for L<sub>0</sub> were determined using pH-spectrophotometric titration, and the other two carboxylic groups were used from the literature.<sup>56</sup> The first two protonation constants from our data were 8.18 and 5.77 assigned to the amine and pyridine groups, respectively. These values were slightly different from the previously reported values of 9.57 and 5.99,<sup>56</sup> respectively, which were obtained by potentiometry. Unfortunately, the ligands L<sub>0</sub>–L<sub>5</sub> have poor water solubility, and reliable potentiometry titrations could not be performed.<sup>67</sup>

For L<sub>1</sub>, the predominant species at pH  $\sim$ 3.5 has an absorption band at 325 nm, while increasing the pH to  $\sim$ 7 generates another species with an absorption band at 331 nm. A further increase in the pH results in a decrease of the 331 nm

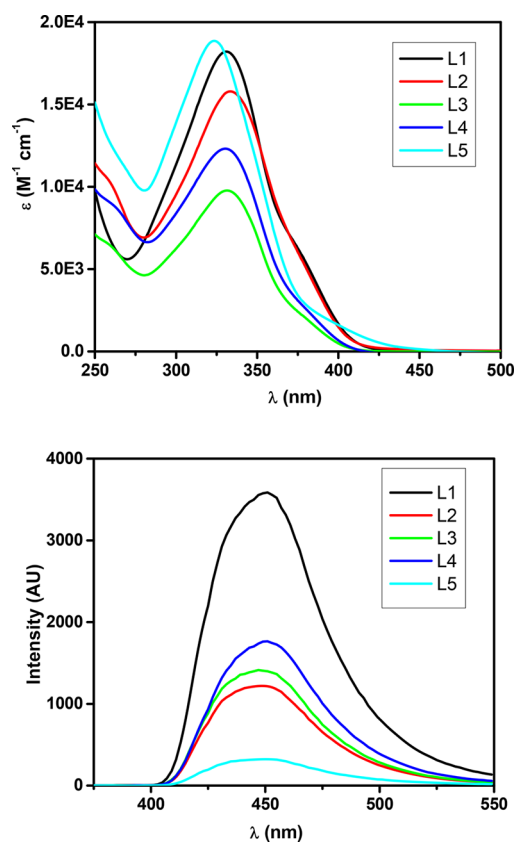


**Figure 1.** Absorption (top) and fluorescence (bottom) spectra of the BFCs L<sub>1</sub>–L<sub>5</sub> in phosphate-buffered saline.

feature and the formation of a new band at 375 nm that reaches a maximum intensity at pH  $\sim$ 11 (Figure 2). On the basis of these changes in the spectra, simulation of the data afforded four pK<sub>a</sub> values of 3.78, 6.35, 8.27, and 9.34. Analogous spectrophotometric titrations were carried out for L<sub>2</sub>–L<sub>5</sub>, and simulations reveal similar speciation diagrams (Figures S1–S5)<sup>63</sup> and corresponding pK<sub>a</sub> values (Table 1). Overall, the highest pK<sub>a</sub> value can be assigned to deprotonation of the phenol group, while the other three pK<sub>a</sub> values likely correspond to deprotonation of the pyridinium and ammonium groups. It is worth mentioning that 1,4,7-triazacyclononane has been reported to exhibit two pK<sub>a</sub> values of 6.88 and 10.42.<sup>49</sup> The pK<sub>a</sub> values of the amine groups in L<sub>1</sub>–L<sub>5</sub> can be similar or even higher. While it is possible that the highest value that we observe may be due to an amine group, based on the dramatic spectral changes observed in this high pH range, we have assigned this pK<sub>a</sub> value to phenol deprotonation. Finally, it is important to note that pH UV–vis titrations may not be the optimal approach for obtaining accurate acidity constants for complex systems such as L<sub>5</sub>, so the pK<sub>a</sub> values obtained herein may be slightly less reliable.<sup>56</sup>

**Stability Constant Determination.** To determine the affinity of these ligands toward Cu<sup>2+</sup>, UV–vis pH-spectrophotometric titrations were performed. Protonation constants of ligands and deprotonation of metal-bound H<sub>2</sub>O molecules were included in the calculations to determine the corresponding stability constants. For L<sub>0</sub>, no change in the UV–vis spectrum was observed in the 3–11 pH range, suggesting that, after Cu<sup>2+</sup> chelation, the complex does not undergo deprotonation that affects the UV–vis spectrum. During the pH-spectrophotometric titration of L<sub>1</sub> and Cu<sup>2+</sup>, no free Cu<sup>2+</sup> was observed even

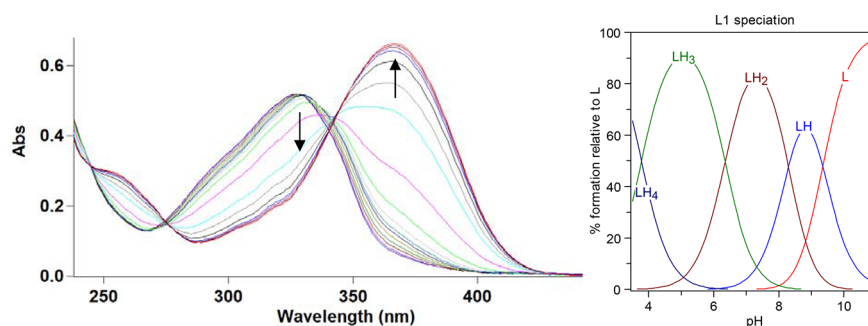


**Figure 2.** Variable-pH (3–11) UV–vis spectra of  $L_1$  ( $50 \mu\text{M}$ ,  $25^\circ\text{C}$ , and  $I = 0.1 \text{ M NaCl}$ ) and the species distribution plot.

**Table 1.** List of  $\text{p}K_a$  Values of  $L_0$ – $L_5$

	$L_0$	$L_1$	$L_2$	$L_3$	$L_4$	$L_5$
$[\text{HL}1]/[\text{L}1]^-$ ( $\text{p}K_{a4}$ )	8.18(8)	9.34(1)	10.14(1)	9.60(1)	9.98(2)	10.65(3)
$[\text{H}_2\text{L}1]^+ / [\text{HL}1]$ ( $\text{p}K_{a3}$ )	5.77(6)	8.27(2)	9.34(3)	8.02(1)	8.71(3)	8.22(4)
$[\text{H}_3\text{L}1]^{2+} / [\text{H}_2\text{L}1]^+$ ( $\text{p}K_{a2}$ )	2.59 <sup>a</sup>	6.35(2)	7.84(4)	5.61(5)	6.93(4)	7.39(5)
$[\text{H}_4\text{L}1]^{3+} / [\text{H}_3\text{L}1]^{2+}$ ( $\text{p}K_{a1}$ )	2.05 <sup>a</sup>	3.78(3)	5.14(4)	4.80(8)	4.57(4)	4.35(6)

<sup>a</sup>From ref 56.

at pH values as low as 3, indicating a high binding affinity of  $L_1$  toward  $\text{Cu}^{2+}$  (Figure S6).<sup>63</sup> It is important to note that the presence of less than 10% of free metal ions at the beginning of the titration can lead to less reliable stability constants, and alternate NMR titrations<sup>56</sup> or competitive titrations with other strong chelators<sup>68</sup> are expected to give more accurate stability constant values. However, the calculated  $\log K$  value of  $\sim 32$  at least suggests that the deprotonated  $L_1$  ligand exhibits a very high binding affinity for  $\text{Cu}^{2+}$  (Table 2), which is expected

**Table 2.** Stability Constants ( $\log K$  Values) of the Copper Complexes of  $L_1$ – $L_4$ , As Determined from pH-Spectrophotometric Titrations

reaction	$\log K$			
	$L_1$	$L_2$	$L_3$	$L_4$
$\text{M}^{2+} + \text{HL} = [\text{MHL}]^{+2}$		2.88(1)	4.01(1)	3.01(1)
$\text{M}^{2+} + \text{L}^- = [\text{ML}]^+$	31.96(6)	27.09(4)	27.22(4)	30.10(5)
$[\text{ML}(\text{H}_2\text{O})]^{+1} = [\text{ML}(\text{OH})] + \text{H}^+$	10.14(6)			

given the macrocyclic nature of the tacn chelating fragment. The small change in the spectra occurring from pH 3 to 9.5 and the shift from 350 to 358 nm are tentatively assigned to

deprotonation of the metal-coordinated  $\text{H}_2\text{O}$  molecule (Figure S6).<sup>63</sup>

The titration of  $L_2$  with  $\text{Cu}^{2+}$  reveals an absorption band at  $\sim 330 \text{ nm}$  at low pH values of 3–4, while at higher pH values, an absorption band at  $400 \text{ nm}$  develops that is tentatively assigned to a phenolate-to- $\text{Cu}^{2+}$  charge-transfer (CT) band and suggests copper complex formation (Figure 3). Simulation of the titration data reveals a stability constant of  $\log K = 27$  for the deprotonated  $L_2$  ligand, which is slightly lower than that found for  $L_1$ , yet it still supports a very high binding affinity for copper. Similarly, for all of the other BFCs  $L_3$ – $L_5$ , a similar behavior was observed in the pH-spectrophotometric titrations with  $\text{Cu}^{2+}$  (Figures S7–S9).<sup>63</sup> All of the BFCs exhibit high binding affinities toward  $\text{Cu}^{2+}$ , as indicated by high stability constants of  $\log K$  values of 27–30 (Table 2). While these values seem extremely high, previous studies have reported high stability constants of  $\log K = 14$ – $27$  for other chelates using the same tacn or N4 metal-binding framework.<sup>48,49</sup> The presence of an additional phenolate metal-binding arm from the amyloid-binding moiety can lead to the observed increase in affinity, which can thus be viewed as a synergistic effect specific for these bifunctional chelators. As expected, the addition of the acetate arm in  $L_4$  increases further the affinity for Cu by about three log units. Notably, along with tacn, the tetradentate N4 macrocyclic ring exhibits a high affinity for  $\text{Cu}^{2+}$  (Table 2).

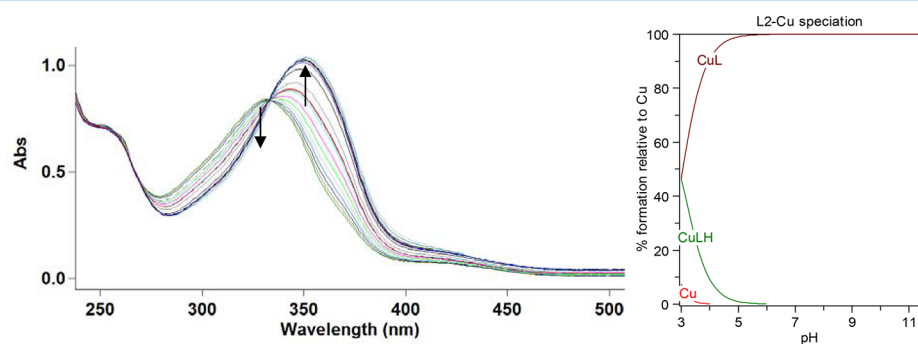


**Figure 3.** Variable-pH (pH 3–11) UV–vis spectra of a  $L_2$  and  $\text{Cu}^{2+}$  system ( $[\text{L}_2] = [\text{Cu}^{2+}] = 50 \mu\text{M}$ ,  $25^\circ\text{C}$ , and  $I = 0.1 \text{ M NaCl}$ ) and the species distribution plot.

Finally, titration of  $L_5$  and  $Cu^{2+}$  reveals an absorption band at  $\sim 330$  nm in the 3–4 pH range, while a band at 400 nm grows in as the pH is increased, suggestive of a phenolate-to- $Cu^{2+}$  CT transition, followed by the likely deprotonation of the second phenol group at pH  $\sim 10$ . This behavior suggests that at neutral pH values one phenolate group coordinates to the Cu center while the other does not. While a high Cu binding affinity for  $L_5$  is suggested by these data, the complex spectral changes could not be fitted in *HYPSPPEC* to give meaningful stability constants, most likely because of the presence of protonation constants that were too close in value to each other, as well as the possible formation of higher-nuclearity complexes (see below). However, it is expected that  $L_5$  exhibits stability constants similar to those observed for  $L_1$ – $L_4$ .

For a better comparison of the  $Cu^{2+}$  binding affinities of these BFCs, pCu ( $-\log [Cu]_{free}$ ) values were calculated at two pH values (Table 3). Interestingly, the pCu values of the BFCs

**Table 3.** Calculated pCu ( $-\log [Cu]_{free}$ ) for a Solution Containing a 1:1 Metal/Ligand Mixture ( $[Cu^{2+}]_{tot} = [chelator]_{tot} = 50 \mu M$ )

	$L_1$	$L_2$	$L_3$	$L_4$	DTPA <sup>a</sup>
pH 6.6	12.8	11.7	11.5	12.0	9.7
pH 7.4	13.3	13.5	12.3	14.1	10.7

<sup>a</sup>Reference 69.

$L_1$ – $L_4$  with a macrocyclic chelating group are significantly higher than the nonmacrocyclic BFCs that we reported previously,<sup>51</sup> as well as the standard strong chelators such as diethylenetriaminepentacetic acid (DTPA).<sup>69</sup> However, these values are quite in the range of similar systems studied before for copper chelation.<sup>48–50</sup> During the titration experiments, the spectral changes observed were immediate, suggesting a fast copper chelation. This is important for efficient  $^{64}Cu$  radiolabeling, which requires fast complexation and is also supported by rapid complexation and isolation of the corresponding copper(2+) complexes (see the Experimental Section). Overall, while thorough spectrophotometric titrations for a wider pH range could not be performed given the limited water solubility of these ligands, these results do strongly suggest that the BFCs  $L_1$ – $L_5$  should be suitable as  $^{64}Cu$  chelating agents, as supported by our recently published PET imaging studies.<sup>70</sup>

**Isolation and Characterization of Copper(2+) Complexes.** The tetranuclear  $L_0$ -Cu complex **1** was prepared by reacting  $L_0$  with  $Cu(ClO_4)_2$  in aqueous media at pH  $\sim 4$ –5. Evaporation of the solvent afforded a green solid, which was dissolved in MeCN and, upon slow evaporation, yielded X-ray-quality crystals. The mononuclear  $L_0$ -Cu complex **2** was obtained when **1** was dissolved in 1 M HCl and left to slowly evaporate for several days. Importantly, demetalation did not occur in such a highly acidic medium, suggesting that the N4 macrocycle is a strong chelator for Cu and thus could potentially be used in vivo.<sup>28,68</sup> This increased acid stability of **2** inspired us to employ N4-based chelators to develop bifunctional compounds (BFC) that could be suitable for PET imaging applications upon labeling with  $^{64}Cu$ . Moreover, copper complexes of the BFCs  $L_1$ – $L_5$  could be isolated when stoichiometric amounts of ligand and  $Cu^{2+}$  salt were reacted in MeOH or MeCN in the presence of the base needed to deprotonate the phenol groups, which led to the formation of brown-red copper complexes that were characterized by X-ray crystallography, elemental analysis, UV–vis spectroscopy, ESI-

MS, EPR spectroscopy, and cyclic voltammetry (CV; see below). Further characterization of these complexes by Job's plot analysis reveals that in solution the species with 1:1 metal/ligand stoichiometry are most predominant (Figures S10–S14).<sup>63</sup> However, in the solid state, complexes with different nuclearities are obtained (Scheme 2). While  $L_1$  forms a mononuclear complex with both  $Cu^{2+}$  (**3**) and  $Zn^{2+}$  (**4**),  $L_2$  forms with  $Cu^{2+}$  a dinuclear complex **5**. In addition, the ligands  $L_3$  and  $L_4$  form with  $Cu^{2+}$  mononuclear complexes **6** and **7**, respectively, while ligand  $L_5$  with  $Cu^{2+}$  yields a trinuclear complex **8** with a 2:3 metal/ligand stoichiometry, as shown from the X-ray structure determination (see below). For all copper complexes **2**–**8**, a d–d absorption band was observed in the 600–800 nm range, along with more intense phenolate-to- $Cu^{2+}$  CT bands in the 400–600 nm range (Figures S15–S20).<sup>63</sup>

**X-ray Structures.** The X-ray structure of **1** suggests a highly symmetric tetranuclear complex in the tetragonal  $I4_1/a$  space group (Figure 4, top). Each Cu center adopts a distorted

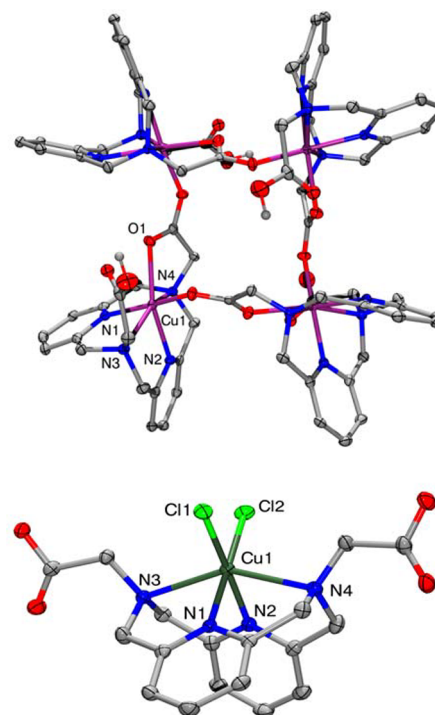


**Figure 4.** ORTEP plots of the tetracations of **1** (top) and **2** (bottom) at the 30% probability level. Perchlorate anions, solvent molecules, and H atoms are omitted for clarity. Selected bond lengths (Å) for **1**: Cu1–N1 1.956(3), Cu1–N2 2.194(3), Cu1–N3 2.250(3), Cu1–N4 2.314(3), Cu1–O1 2.191(2), Cu1–O2 1.901(2). Selected bond lengths (Å) for **2**: Cu1–N1 2.0271(19), Cu1–N2 2.0430(19), Cu1–N3 2.3984(19), Cu1–N4 2.3487(19), Cu1–Cl1 2.3145(6), Cu1–Cl2 2.2861(6).

octahedral geometry with coordination to the two pyridine and two amine N atoms of the N4 macrocycle and two carboxylate O atoms. One carboxylate is part of the same  $L_0$  ligand, while the other O atom belongs to another  $L_0$  ligand of the tetrameric complex. Notably, one acetate arm from each  $L_0$  ligand remains uncoordinated and in the protonated state. The bond distances between the Cu center and the N atoms of N4 are in the range of 1.953(3)–2.314(3) Å, typical for N4-Cu complexes.<sup>71</sup> The

two carboxylate O1 and O2 atoms are coordinated to Cu at distances of 2.191(2) and 1.901(2) Å, respectively.

The mononuclear complex **2** was obtained by recrystallization of **1** in 1 M HCl. Its X-ray structure reveals a Cu center in a distorted octahedral coordination that interacts with the four N atoms of N4 and two chloride anions (Figure 4, bottom). The Cu–N<sub>pyridine</sub> bond distances are 2.0271(19) and 2.0430(19) Å, while the amine N atoms occupy the axial positions and exhibit longer Cu–N<sub>amine</sub> bond distances of 2.3984(19) and 2.3487(19) Å. The chloride anions occupy the other equatorial positions at distances of 2.3984(19) and 2.3487(19) Å from the Cu center, respectively. In general, the bond distances between the Cu center and the N atoms of N4 in **2** are longer than those in **1**, likely because of the “opening” of the N4 chelate to allow for the intra- and intermolecular interactions of the Cu center with the acetate arms from two different L<sub>0</sub> ligands.

Although X-ray-quality crystals for the L<sub>1</sub>-Cu complex **3** could not be obtained, the L<sub>1</sub>-Zn complex **4** was synthesized and single crystals were obtained by the slow evaporation of a MeOH/H<sub>2</sub>O solution. In **4**, the Zn center exhibits a N<sub>3</sub>O<sub>3</sub> octahedral coordination environment, with three N atoms from the tacn macrocycle, one phenolate O atom, and two O atoms from the two coordinated H<sub>2</sub>O molecules (Figure 5). The Zn–

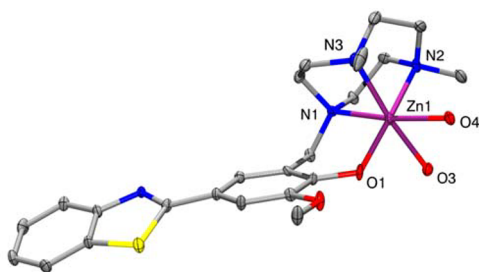


**Figure 5.** ORTEP plot of the cation of **4** at the 30% probability level. Perchlorate anions and H atoms are omitted for clarity. Selected bond lengths (Å) for **4**: Zn1–N1 2.163(5), Zn1–N2 2.177(5), Zn1–N3 2.185(5), Zn1–O1 2.013(4), Zn1–O3 2.258(4), Zn1–O4 2.084(4).

N bond distances are in the range of 2.163(5)–2.185(5) Å, while the Zn–N bond distances are in the range of 2.013(4)–2.258(4) Å. It is expected that the L<sub>1</sub>-Cu complex **3** may exhibit a more distorted octahedral or likely a five-coordinate geometry because of the Jahn–Teller effect, while the formation of a dinuclear complex in the solid state could not be excluded (see below).

Single crystals of the L<sub>2</sub>-Cu complex **5** were obtained by ether diffusion into a CH<sub>2</sub>Cl<sub>2</sub> solution of **5**. Interestingly, the complex consists of a discrete centrosymmetric [(L<sub>2</sub>)Cu]<sub>2</sub> unit, where two phenolates are acting as bridging ligands between the two Cu centers (Figure 6). Each Cu center adopts a distorted octahedral geometry, with the pyridyl N atoms and the phenolate O atoms occupying the equatorial plane, while the amine N atoms take the axial positions. Notably, the two Cu centers are separated by 3.125 Å, and the Cu–O–Cu angle is 77.125°, which is the shortest phenolate bridging angle observed for diphenoxo-bridged copper complexes.<sup>72</sup> The formation of such a dinuclear copper complex for L<sub>2</sub> may be due to the lack of an N substituent on the second amine N atom of the N4 ligand, which limits steric clashes between the two L<sub>2</sub> molecules. By comparison, the reactions of the ligands L<sub>3</sub> and L<sub>4</sub> with Cu<sup>2+</sup> yield mononuclear complexes **6** and **7**.

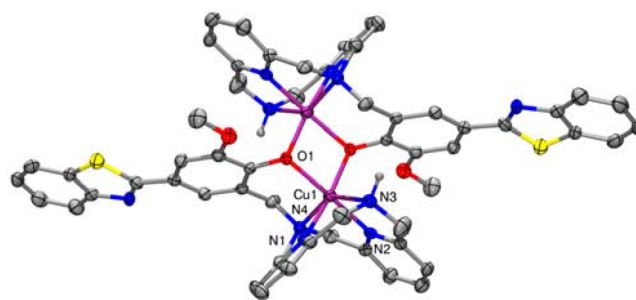


**Figure 6.** ORTEP plot of the dication of **5** at the 30% probability level. Perchlorate anions and H atoms are omitted for clarity. Selected bond lengths (Å) for **5**: Cu1–N1 2.002(4), Cu1–N2 2.015(4), Cu1–N3 2.387(4), Cu1–N4 2.283(4), Cu1–O1 2.002(3), Cu1–O2 1.995(3). Reproduced from ref 61.

Although these species could not be structurally characterized, it is expected that the presence of the bulkier methyl or acetate N substituent in L<sub>3</sub> and L<sub>4</sub> should sterically preclude the formation of dinuclear, phenolate-bridged complexes.

The identity of ligand L<sub>5</sub> was confirmed by X-ray crystallography (Figure S21),<sup>63</sup> and single crystals of the L<sub>5</sub>-Cu complex **8** were obtained upon the slow evaporation from MeOH. Interestingly, the X-ray structure reveals a linear, trinuclear copper complex that is supported by only two L<sub>5</sub> molecules that complete the distorted octahedral coordination environment of the two terminal Cu centers (Figure 7), while

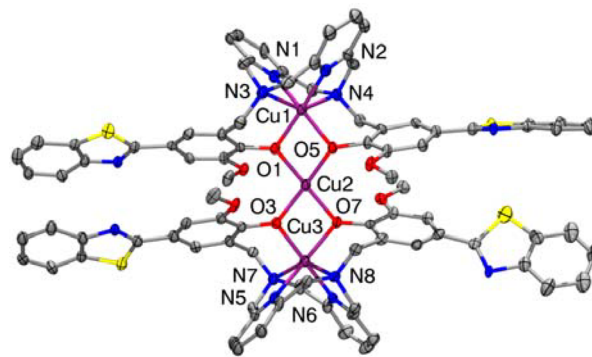


**Figure 7.** ORTEP plot of the dication of **8** at the 30% probability level. Perchlorate anions and H atoms are omitted for clarity. Selected bond lengths (Å) for **8**: Cu1–N1 2.039(13), Cu1–N2 2.006(16), Cu1–N3 2.302(15), Cu1–N4 2.311(13), Cu1–O1 1.940(11), Cu1–O5 1.998(10), Cu2–O1 1.930(10), Cu2–O3 1.937(10), Cu2–O5 1.940(11), Cu2–O7 1.950(10), Cu2–O9 2.433(16), Cu3–N5 2.068(14), Cu3–N6 1.977(13), Cu3–N7 2.259(14), Cu3–N8 2.323(13), Cu3–O3 1.918(10), Cu3–O7 2.025(11), Cu1–Cu2 3.044(3), Cu2–Cu3 3.054(3). Reproduced from ref 61.

the square-pyramidal central Cu ion is coordinated by the four phenolate O atoms from the two L<sub>5</sub> molecules and a H<sub>2</sub>O molecule. As expected, the amine N atoms occupy the axial positions of the two terminal Cu centers, at distances of ~2.30 Å, while the pyridyl N atoms and phenolate O atoms are found in the equatorial plane. The Cu1–Cu2 distance is 3.044(3) Å and the Cu2–Cu3 distance is 3.054(3) Å, similar to other diphenoxo-bridged complexes.<sup>73</sup> Notably, the Job’s plot analysis of **8** suggests the presence in an aqueous solution of a species with a 1:1 metal/ligand stoichiometry, which is expected given that H<sub>2</sub>O molecules should help dissociate the interactions between the central Cu ion and the phenolate O atoms.



**EPR Spectra of Copper Complexes.** To further characterize the synthesized copper complexes, their X-band EPR spectra were recorded in frozen glasses at 77 K. The EPR spectrum of the  $L_0$ -Cu mononuclear complex **2** in a 2:3 (v/v) 1 M HCl/glycerol frozen solution reveals a pseudoaxial EPR pattern with three different  $g$  values:  $g_x = 2.290$ ,  $g_y = 2.075$ , and  $g_z = 2.034$  (Figure 8, top). Similarly, the EPR spectrum of the

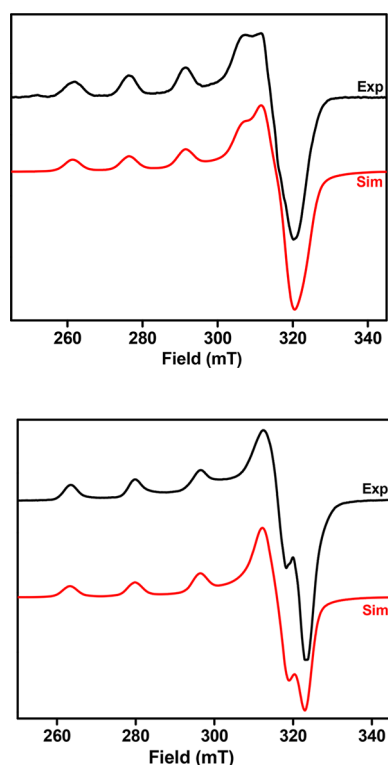


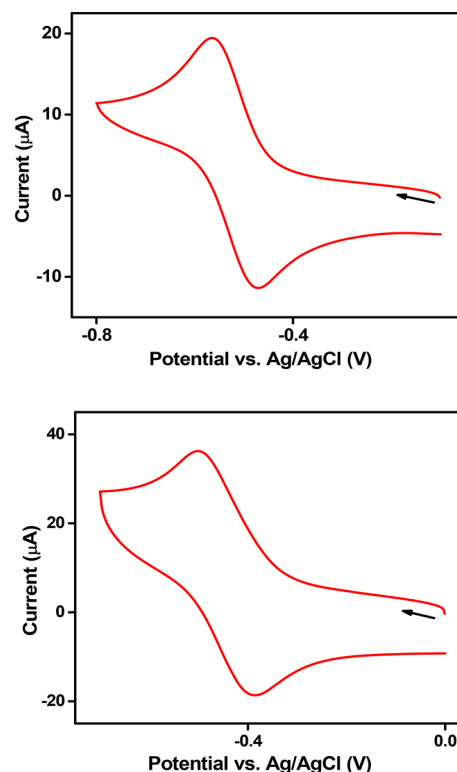
**Figure 8.** EPR spectra of the  $L_0$ -Cu mononuclear complex **2** in 2:3 1 M HCl/glycerol (top) and the  $L_1$ -Cu complex **3** in 1:3 MeCN/PrCN (bottom) at 77 K. The following parameters were used for the simulations: **2**,  $g_x = 2.290$ ,  $A_x(\text{Cu}) = 150$  G,  $g_y = 2.075$ , and  $g_z = 2.034$ ; **3**,  $g_x = 2.256$ ,  $A_x(\text{Cu}) = 165$  G,  $g_y = 2.075$ , and  $g_z = 2.045$ .

$L_1$ -Cu complex **3** in 1:3 MeCN/PrCN reveals a pseudoaxial EPR pattern with three different  $g$  values:  $g_x = 2.256$ ,  $g_y = 2.075$ , and  $g_z = 2.045$  (Figure 8, bottom). In general, the  $R$  parameter [ $R = (g_y - g_z)/(g_x - g_y)$  with  $g_x > g_y > g_z$ ] can be indicative of the predominance of the  $d_{z^2}$  or  $d_{x^2-y^2}$  orbital in the ground state of the unpaired electron of the  $\text{Cu}^{2+}$  ion. When  $R > 1$ , the greater contribution to the ground state arises from the  $d_{z^2}$  orbital, while when  $R < 1$ , the greater contribution to the ground state comes from the  $d_{x^2-y^2}$  orbital.<sup>74,75</sup> The  $R$  values of 0.19 determined for **2** and 0.16 for **3** are indicative of a predominantly  $d_{x^2-y^2}$  ground state, which is characteristic for copper(II) complexes with slightly rhombic symmetry and elongation of the axial bonds.<sup>48,76–78</sup> The X-ray structure of **2** (see above) indeed suggests that all six metal–ligand bond distances are different and the Cu center is an axially elongated coordination environment, with the amine N atoms found in the axial positions. Because **3** has a EPR spectrum similar to that of **2**, it can be assumed that the Cu center in **3** adopts an axially elongated geometry as well.

Because the  $L_2$ -Cu complex **5** is a diphenoxo-bridged dicopper complex, no EPR spectrum for this complex was observed, likely because of an antiferromagnetic coupling between the two Cu centers through the phenoxide bridging

ligands. Finally, the  $L_3$ -Cu complex **6** and  $L_4$ -Cu complex **7**, as well as the  $L_5$ -Cu complex **8**, exhibit intense EPR spectra (Figures S22–S24),<sup>63</sup> suggesting that these complexes exist in solution as mononuclear species. However, the presence of closely spaced  $g$  values and hyperfine coupling to copper ( $I = 3/2$ ) did not allow for an acceptable simulation of these EPR spectra.

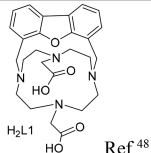
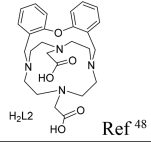
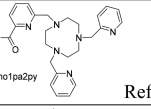
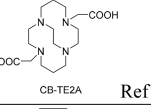
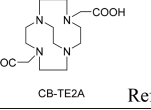
**Electrochemistry of Copper Complexes.** The use of copper(II) complexes as radiopharmaceuticals could be hampered by demetalation of these complexes in vivo. The facile reduction of  $\text{Cu}^{\text{II}}$  to  $\text{Cu}^{\text{I}}$  by bioreductants in these complexes could facilitate the demetalation step, and thus complexes that exhibit more negative  $\text{Cu}^{\text{II}}/\text{Cu}^{\text{I}}$  redox potentials are desired. We set out to determine the  $\text{Cu}^{\text{II}}/\text{Cu}^{\text{I}}$  redox potentials of the synthesized copper complexes using CV in aqueous media at neutral pH to determine the  $\text{Cu}^{\text{II}}/\text{Cu}^{\text{I}}$  redox potentials versus Ag/AgCl reference electrode. The cyclic voltammograms of the  $L_0$ -Cu complex **2** and the  $L_2$ -Cu complex **5** are shown in Figure 9, while the cyclic voltammo-



**Figure 9.** Cyclic voltammograms of the  $L_0$ -Cu complex **2** (top; 0.1 M NaOAc/ $\text{H}_2\text{O}$ ) and the  $L_2$ -Cu complex **5** (bottom; 0.1 M NaOAc in 1:1 MeCN/ $\text{H}_2\text{O}$ ) at 100  $\text{mV s}^{-1}$  scan rates.

grams of all of the copper complexes **3**, **6**, **7**, and **8** are shown in Figures S25–S28.<sup>63</sup> The cyclic voltammograms of the  $L_0$ -Cu complex **2**, the  $L_2$ -Cu complex **5**, the  $L_3$ -Cu complex **6**, and the  $L_4$ -Cu complex **7** show quasi-reversible  $\text{Cu}^{\text{II}}/\text{Cu}^{\text{I}}$  redox behavior, which indicates that these ligands can accommodate a  $\text{Cu}^{\text{I}}$  oxidation state as well. The cyclic voltammogram of the  $L_1$ -Cu complex **3** was irreversible (Figure S25),<sup>63</sup> while the cyclic voltammogram of the  $L_5$ -Cu complex **8** did not show a clear cathodic peak, suggesting that the  $\text{Cu}^{\text{I}}$  oxidation state is quite unfavored because of the presence of two bridging phenolate O-atom donors. The electrochemical properties of these copper complexes are summarized in Table 4 and

**Table 4. Electrochemical Parameters for Complexes 2–8 and Other Relevant Copper Complexes**

Complex	E <sub>pc</sub> (mV vs. Ag/AgCl)	Nature of wave	Reference
L <sub>0</sub> -Cu (2)	-566	Quasi-reversible	This work
L <sub>1</sub> -Cu (3)	-670	Irreversible	This work
L <sub>2</sub> -Cu (5)	-490	Quasi-reversible	This work
L <sub>3</sub> -Cu (6)	-456	Irreversible	This work
L <sub>4</sub> -Cu (7)	-570	Quasi-reversible	This work
L <sub>5</sub> -Cu (8)	-920	Irreversible	This work
Cu-H2L1	-652	Irreversible	 H <sub>2</sub> L1 Ref <sup>48</sup>
Cu-H2L2	-644	Irreversible	 H <sub>2</sub> L2 Ref <sup>48</sup>
Cu-No1pa2py	-675	Quasi-reversible	 Hno1pa2py Ref <sup>49</sup>
Cu-CB-TE2A	-1080	Quasi-reversible	 CB-TE2A Ref <sup>79</sup>
Cu-CB-DO2A	-1000	Irreversible	 CB-TE2A Ref <sup>79</sup>

compared to other copper complexes used for similar imaging applications. Interestingly, all of the Cu<sup>II</sup>/Cu<sup>I</sup> redox potentials are fairly low in the range of -490 to -920 mV, similar to other copper complexes that have shown promise for radiolabeling and their potential use in in vivo imaging applications.<sup>48,49,79</sup>

**Effect of L<sub>1</sub>–L<sub>5</sub> on Aβ Aggregation.** The BFCs L<sub>1</sub>–L<sub>5</sub> were also evaluated for their ability to inhibit Aβ aggregation, in both the absence and presence of Cu<sup>2+</sup> or Zn<sup>2+</sup> ions. We have tested their effect on the inhibition of aggregation of the Aβ<sub>42</sub> peptide, which was shown to be more prone to aggregate and form neurotoxic soluble Aβ oligomers.<sup>80–82</sup> Freshly prepared monomeric Aβ<sub>42</sub> solutions were treated with metal ions and/or BFCs, incubated for 24 h at 37 °C, and then analyzed by TEM and native gel electrophoresis/Western blotting. TEM analysis allows characterization of the larger, insoluble Aβ aggregates, while native gel electrophoresis/Western blotting probes the presence of smaller, soluble Aβ aggregates and their molecular weight distribution. As shown previously,<sup>51</sup> the Aβ<sub>42</sub> peptide forms large fibrils upon incubation for 24 h at 37 °C, and the metal ions affect the fibrilization process. Gratifyingly, all of the BFCs L<sub>1</sub>–L<sub>5</sub> show good inhibition of the Aβ<sub>42</sub> aggregation process, in both the absence or presence of Cu<sup>2+</sup> or Zn<sup>2+</sup>. Western blot analysis shows that all of the BFCs tested reduce the formation of both insoluble Aβ<sub>42</sub> aggregates (Figure 10) and large, neurotoxic soluble Aβ<sub>42</sub> oligomers (Figure 11). Thus,

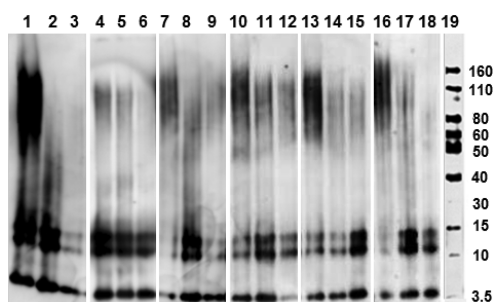


**Figure 11.** Native gel electrophoresis/Western blot analysis of the inhibition of Aβ<sub>42</sub> aggregation ([Aβ] = 25 μM, [M<sup>2+</sup>] = 25 μM, [compound] = 50 μM, 24 h, and 37 °C). Lanes: 1, Aβ; 2, Aβ + Cu; 3, Aβ + Zn; 4, Aβ + L<sub>1</sub>; 5, Aβ + Cu + L<sub>1</sub>; 6, Aβ + Zn + L<sub>1</sub>; 7, Aβ + L<sub>2</sub>; 8, Aβ + Cu + L<sub>2</sub>; 9, Aβ + Zn + L<sub>2</sub>; 10, Aβ + L<sub>3</sub>; 11, Aβ + Cu + L<sub>3</sub>; 12, Aβ + Zn + L<sub>3</sub>; 13, Aβ + L<sub>4</sub>; 14, Aβ + Cu + L<sub>4</sub>; 15, Aβ + Zn + L<sub>4</sub>; 16, Aβ + L<sub>5</sub>; 17, Aβ + Cu + L<sub>5</sub>; 18, Aβ + Zn + L<sub>5</sub>; 19, MW markers. Reproduced from ref 61.

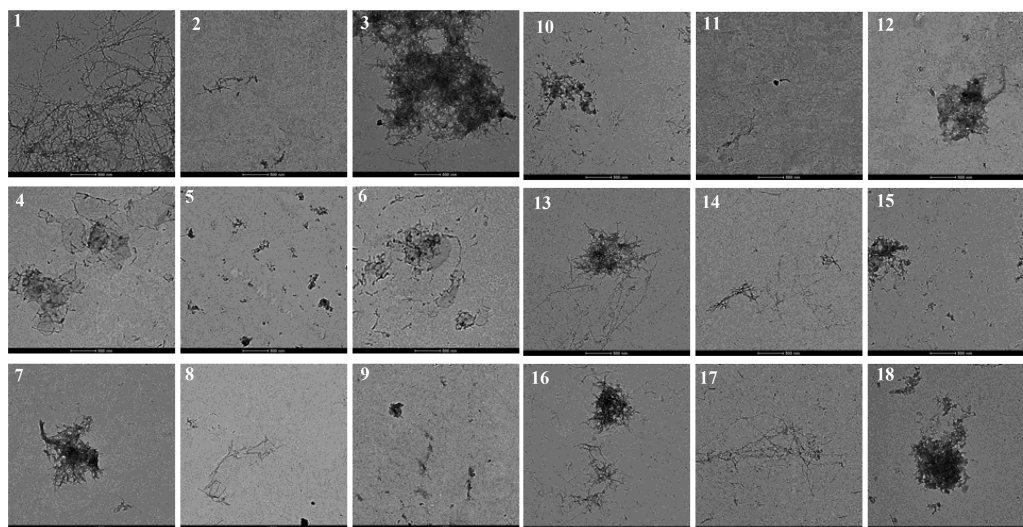


**Figure 10.** TEM images of Aβ<sub>42</sub> species from inhibition experiments ([Aβ] = 25 μM, [M<sup>2+</sup>] = 25 μM, [BFC] = 25 μM, 24 h, and 37 °C). All scale bars represent 500 nm. Panels: 1, Aβ; 2, Aβ + Cu; 3, Aβ + Zn; 4, Aβ + L<sub>1</sub>; 5, Aβ + Cu + L<sub>1</sub>; 6, Aβ + Zn + L<sub>1</sub>; 7, Aβ + L<sub>2</sub>; 8, Aβ + Cu + L<sub>2</sub>; 9, Aβ + Zn + L<sub>2</sub>; 10, Aβ + L<sub>3</sub>; 11, Aβ + Cu + L<sub>3</sub>; 12, Aβ + Zn + L<sub>3</sub>; 13, Aβ + L<sub>4</sub>; 14, Aβ + Cu + L<sub>4</sub>; 15, Aβ + Zn + L<sub>4</sub>; 16, Aβ + L<sub>5</sub>; 17, Aβ + Cu + L<sub>5</sub>; 18, Aβ + Zn + L<sub>5</sub>. Reproduced from ref 61.

none of the BFCs  $L_1$ – $L_5$  leads to an enhanced  $A\beta_{42}$  oligomerization in the absence or presence of metal ions and thus should not exhibit any neurotoxic side effects in in vivo studies.

## DISCUSSION

Because the in vivo stability of copper complexes is a critical factor for the design of optimal ligands  $^{64}\text{Cu}$  PET imaging applications, significant research has been devoted to the development of ligands that can form stable complexes of  $^{64}\text{Cu}$ . The use of macrocyclic ligands cyclam and cyclen, 1,4,7,10-tetraazacyclododecane-1,4,7,10-tetraacetic acid, triethylenetetramine, cross-bridged cyclam, and many other cyclic polyamines has been explored for this purpose,<sup>28</sup> and many of these chelates have linked with targeting groups such as proteins, peptides, or antibodies to develop bifunctional imaging agents.<sup>32,83</sup> For example, a family of bis(thiosemicarbazone) ligands, derived from 1,2-diones, have been under intense investigation as delivery vehicles for radioactive copper isotopes because they form stable and neutral, membrane-permeable copper complexes.<sup>68</sup> However, in the context of neurodegenerative diseases like AD, to the best of our knowledge, only one recent report by Donnelly et al. describes the use of bifunctional  $^{64}\text{Cu}$ -labeled compounds that selectively bind  $A\beta$  aggregates.<sup>68</sup> In that report bis(thiosemicarbazone) ligands appended with an amyloid-targeting stilbene functional group were employed, and their Cu complexes were shown to bind selectively to  $A\beta$  plaques in post-mortem samples of human brains from AD subjects. In the same report, the authors also employed a bis(thiosemicarbazone) ligand containing a benzothiazole moiety, yet it did not exhibit an appreciable affinity for  $A\beta$  plaques and thus it was not used in imaging studies.<sup>68</sup>

Benzothiazole- and stilbene-derived molecules display a high affinity for  $A\beta$  fibrils, most likely because these molecules interact with the hydrophobic pockets of amyloid fibrils through hydrophobic and  $\pi$ – $\pi$  interactions. We have been using 2-phenylbenzothiazole-derived metal-chelating BFCs with high affinity for  $A\beta$  aggregates to control the metal-mediated aggregation and neurotoxicity of soluble  $A\beta$  oligomers.<sup>51,66</sup> These bifunctional chelators are proposed to mediate interaction of the metal ions with the  $A\beta$  species and are of interest as potential therapeutics.<sup>84,85</sup> Herein, we employed tacn and pyridinophane (N4) macrocycles, which are very strong copper chelators, and linked them with the amyloid-binding 2-phenylbenzothiazole fragment through Mannich reactions. These new BFCs could then be radiolabeled with  $^{64}\text{Cu}$  and thus become amyloid-binding PET imaging agents.

In general, a test to predict whether metal complexes are stable enough for in vivo applications is to investigate whether these complexes withstand demetalation in a strongly acidic medium. Harsh conditions (1–5 M HCl, 50–90 °C) are generally used to test the stability of copper complexes and whether they could be used for  $^{64}\text{Cu}$  radiopharmaceutical applications.<sup>28,49</sup> In our case, we observed that the  $L_0$  ligand rapidly forms a stable copper complex in 1 M HCl, suggesting that the N4-derived ligands can be radiolabeled with  $^{64}\text{Cu}$  under mild conditions. In addition, the resulting  $L_0$ -Cu complex is stable for days in 1 M HCl, suggesting that the N4 framework should instill appreciable kinetic stability of the corresponding complexes.<sup>56</sup> While the copper complexes of the BFCs  $L_2$ – $L_5$  are expected to exhibit slightly lower stability constants than those for  $L_0$ , UV–vis pH titrations reveal the presence of very

few free  $\text{Cu}^{2+}$  ions in solution even at low pH values, thus suggesting their appreciable stability in acidic media. Importantly, we have previously shown that for BFCs related to those described herein, their stability constants for copper complexes are 2–3 orders of magnitude higher than those for the corresponding zinc complexes,<sup>51</sup> thus suggesting that transmetalation with zinc for the copper complexes should not occur to an appreciable extent. In addition, the use of tacn as a metal chelator in the BFC  $L_1$  was inspired from the recently developed metal chelators with exceptional kinetic stability, both ex vivo and in vivo.<sup>49</sup> Finally, our recently published PET imaging and biodistribution studies strongly suggest that the BFCs  $L_1$ – $L_5$  should be suitable as  $^{64}\text{Cu}$  chelating agents,<sup>70</sup> lending support to the coordination chemistry studies described herein.

The solution properties of the ligands  $L_0$ – $L_5$  were investigated in detail, as described above. All ligands exhibit very high stability constants for copper, and thus we can expect these chelators to be useful for Cu PET agents.<sup>61,70</sup> Isolation and characterization of the corresponding copper complexes and their structural characterization enabled us to understand the coordination properties of the BFCs  $L_1$ – $L_5$ . The calculated pCu values suggest that these chelators are stronger chelators than the conventionally used chelators such as DTPA. In addition, the formation of mononuclear complexes in solution with 1:1 metal/ligand stoichiometry is important for the development of low-molecular-weight PET imaging agents that need to cross the blood–brain barrier. Finally, another possible route of demetalation of copper complexes in vivo is the reduction of  $\text{Cu}^{\text{II}}$  to  $\text{Cu}^{\text{I}}$  by bioreductants; an estimated reduction potential of –400 mV versus NHE was determined for the typical bioreductants.<sup>27</sup> CV experiments suggest that all of the copper complexes studied herein have lower reduction potentials than –400 mV and thus are expected to be less prone to reduction and demetalation in vivo.<sup>68</sup>

## CONCLUSIONS

Metal complexes of macrocyclic chelators have increasingly versatile applications in the biomedical sciences, especially in radiopharmaceutical chemistry. The use of  $^{64}\text{Cu}$  radionuclide in PET imaging is a promising application, and one of the current challenges is to develop novel chelators that are able to meet the very strict metal-binding specifications for applications such as PET imaging or radiotherapy. In this report, we have presented the synthesis of five new copper chelators  $L_1$ – $L_5$ . All chelators were prepared in good yields and were characterized by  $^1\text{H}$  and  $^{13}\text{C}$  NMR, UV–vis, and ESI-MS. The BFCs  $L_1$ – $L_5$  were designed to include the amyloid-binding 2-phenylbenzothiazole fragment, and thus upon labeling with  $^{64}\text{Cu}$ , they could be employed as PET imaging agents for the detection of  $A\beta$  aggregates in AD brains. As a first step, we have studied in detail the coordination chemistry of these chelators toward  $\text{Cu}^{2+}$ . The copper complex of  $L_0$  is indefinitely stable in 1 M HCl, from which it can be isolated. In addition, the BFCs  $L_1$ – $L_5$  were shown to exhibit very high stability constants for  $\text{Cu}^{2+}$ , as determined by pH-spectrophotometric titrations. The corresponding copper complexes of these BFCs were isolated, structurally characterized, and probed by UV–vis spectroscopy, EPR spectroscopy, and CV. Overall, these new BFCs are attractive candidates for the design of novel  $^{64}\text{Cu}$ -labeled agents for PET imaging applications in AD.<sup>61,70</sup> Current studies in our laboratories are focused on probing the PET imaging properties of the  $^{64}\text{Cu}$ -labeled BFCs described herein.

## ■ ASSOCIATED CONTENT

## S Supporting Information

The Supporting Information is available free of charge on the ACS Publications website at DOI: 10.1021/acs.inorgchem.7b01883.

pH-spectrophotometric titrations for ligands and copper complexes, Job's plots, UV-vis and EPR spectra and CVs of copper complexes, and X-ray structure characterization details (PDF)

## Accession Codes

CCDC 1563650–1563655 contain the supplementary crystallographic data for this paper. These data can be obtained free of charge via [www.ccdc.cam.ac.uk/data\\_request/cif](http://www.ccdc.cam.ac.uk/data_request/cif), or by emailing [data\\_request@ccdc.cam.ac.uk](mailto:data_request@ccdc.cam.ac.uk), or by contacting The Cambridge Crystallographic Data Centre, 12 Union Road, Cambridge CB2 1EZ, UK; fax: +44 1223 336033.

## ■ AUTHOR INFORMATION

## Corresponding Author

\*E-mail: [mirica@wustl.edu](mailto:mirica@wustl.edu).

ORCID 

Liviu M. Mirica: 0000-0003-0584-9508

## Present Address

<sup>‡</sup>Department of Chemistry, Central University of Rajasthan, NH-8, Bandar Sindri, Ajmer, India 305801.

## Notes

The authors declare no competing financial interest.

## ■ ACKNOWLEDGMENTS

We acknowledge research funding from the NIH (Grant R01GM114588), Alzheimer's Association (Grant NIRG 12-259199), Washington University Alzheimer's Disease Research Center (Grant NIH P50-AG05681), and McDonnell Center for Cellular and Molecular Neurobiology at Washington University School of Medicine.

## ■ REFERENCES

- (1) Alzheimer's Disease Facts and Figures: Annual Report from [www.alz.org](http://www.alz.org), 2017.
- (2) Perrin, R. J.; Fagan, A. M.; Holtzman, D. M. Multimodal techniques for diagnosis and prognosis of Alzheimer's disease. *Nature* **2009**, *461*, 916–922.
- (3) Ferri, C. P.; Prince, M.; Brayne, C.; Brodaty, H.; Fratiglioni, L.; Ganguli, M.; Hall, K.; Hasegawa, K.; Hendrie, H.; Huang, Y.; Jorm, A.; Mathers, C.; Menezes, P. R.; Rimmer, E.; Sczufca, M. Global prevalence of dementia: a Delphi consensus study. *Lancet* **2005**, *366*, 2112–2117.
- (4) Hardy, J. A.; Higgins, G. A. Alzheimer's disease: the amyloid cascade hypothesis. *Science* **1992**, *256*, 184–185.
- (5) Jakob-Roetne, R.; Jacobsen, H. Alzheimer's Disease: From Pathology to Therapeutic Approaches. *Angew. Chem., Int. Ed.* **2009**, *48*, 3030–3059.
- (6) Musiek, E. S.; Holtzman, D. M. Three dimensions of the amyloid hypothesis: time, space and 'wingmen'. *Nat. Neurosci.* **2015**, *18*, 800–806.
- (7) Ising, C.; Stanley, M.; Holtzman, D. M. Current Thinking on the Mechanistic Basis of Alzheimer's and Implications for Drug Development. *Clin. Pharmacol. Ther.* **2015**, *98*, 469–471.
- (8) Mucke, L. NEUROSCIENCE: Alzheimer's disease. *Nature* **2009**, *461*, 895–897.
- (9) Mathis, C. A.; Wang, Y.; Klunk, W. E. Imaging  $\beta$ -amyloid plaques and neurofibrillary tangles in the aging human brain. *Curr. Pharm. Des.* **2004**, *10*, 1469–1492.

(10) Selkoe, D. J. Imaging Alzheimer's amyloid. *Nat. Biotechnol.* **2000**, *18*, 823–824.

(11) Mathis, C. A.; Wang, Y.; Holt, D. P.; Huang, G.-F.; Debnath, M. L.; Klunk, W. E. Synthesis and Evaluation of <sup>11</sup>C-Labeled 6-Substituted 2-Arylbenzothiazoles as Amyloid Imaging Agents. *J. Med. Chem.* **2003**, *46*, 2740–2754.

(12) Klunk, W. E.; Engler, H.; Nordberg, A.; Wang, Y. M.; Blomqvist, G.; Holt, D. P.; Bergstrom, M.; Savitcheva, I.; Huang, G. F.; Estrada, S.; Ausen, B.; Debnath, M. L.; Barletta, J.; Price, J. C.; Sandell, J.; Lopresti, B. J.; Wall, A.; Koivisto, P.; Antoni, G.; Mathis, C. A.; Langstrom, B. Imaging brain amyloid in Alzheimer's disease with Pittsburgh Compound-B. *Ann. Neurol.* **2004**, *55*, 306–319.

(13) Ono, M.; Wilson, A.; Nobrega, J.; Westaway, D.; Verhoeff, P.; Zhuang, Z.-P.; Kung, M.-P.; Kung, H. F. <sup>11</sup>C-labeled stilbene derivatives as A $\beta$ -aggregate-specific PET imaging agents for Alzheimer's disease. *Nucl. Med. Biol.* **2003**, *30*, S65–S71.

(14) Zhang, W.; Oya, S.; Kung, M.-P.; Hou, C.; Maier, D. L.; Kung, H. F. F-18 Polyethyleneglycol stilbenes as PET imaging agents targeting A $\beta$  aggregates in the brain. *Nucl. Med. Biol.* **2005**, *32*, 799–809.

(15) Kudo, Y.; Okamura, N.; Furumoto, S.; Tashiro, M.; Furukawa, K.; Maruyama, M.; Itoh, M.; Iwata, R.; Yanai, K.; Arai, H. 2-(2-[2-Dimethylaminothiazol-5-yl]Ethenyl)-6-(2-[Fluoro]Ethoxy)-Benzoxazole: A Novel PET Agent for In Vivo Detection of Dense Amyloid Plaques in Alzheimer's Disease Patients. *J. Nucl. Med.* **2007**, *48*, 553–561.

(16) Agdeppa, E. D.; Kepe, V.; Liu, J.; Flores-Torres, S.; Satyamurthy, N.; Petric, A.; Cole, G. M.; Small, G. W.; Huang, S. C.; Barrio, J. R. Binding characteristics of radiofluorinated 6-dialkylamino-2-naphthylethylidene derivatives as positron emission tomography imaging probes for beta-amyloid plaques in Alzheimer's disease. *J. Neurosci.* **2001**, *21*, RC189.

(17) Zhang, W.; Kung, M.-P.; Oya, S.; Hou, C.; Kung, H. F. 18F-labeled styrylpyridines as PET agents for amyloid plaque imaging. *Nucl. Med. Biol.* **2007**, *34*, 89–97.

(18) Choi, S. R.; Golding, G.; Zhuang, Z.; Zhang, W.; Lim, N.; Hefti, F.; Benedum, T. E.; Kilbourn, M. R.; Skovronsky, D.; Kung, H. F. Preclinical Properties of 18F-AV-45: A PET Agent for A $\beta$  Plaques in the Brain. *J. Nucl. Med.* **2009**, *50*, 1887–1894.

(19) Nordberg, A. Amyloid imaging in Alzheimer's disease. *Curr. Opin. Neurol.* **2007**, *20*, 398–402.

(20) Archer, H. A.; Edison, P.; Brooks, D. J.; Barnes, J.; Frost, C.; Yeatman, T.; Fox, N. C.; Rossor, M. N. Amyloid load and cerebral atrophy in Alzheimer's disease: an <sup>11</sup>C-PIB positron emission tomography study. *Ann. Neurol.* **2006**, *60*, 145–7.

(21) Kemppainen, N. M.; Aalto, S.; Wilson, I. A.; Nagren, K.; Helin, S.; Bruck, A.; Oikonen, V.; Kailajarvi, M.; Scheinin, M.; Viitanen, M.; Parkkola, R.; Rinne, J. O. Voxel-based analysis of PET amyloid ligand [<sup>11</sup>C]PIB uptake in Alzheimer disease. *Neurology* **2006**, *67*, 1575–80.

(22) Mintun, M. A.; Larossa, G. N.; Sheline, Y. I.; Dence, C. S.; Lee, S. Y.; Mach, R. H.; Klunk, W. E.; Mathis, C. A.; DeKosky, S. T.; Morris, J. C. [<sup>11</sup>C]PIB in a nondemented population: potential antecedent marker of Alzheimer disease. *Neurology* **2006**, *67*, 446–52.

(23) Engler, H.; Forsberg, A.; Almkvist, O.; Blomqvist, G.; Larsson, E.; Savitcheva, I.; Wall, A.; Ringheim, A.; Langstrom, B.; Nordberg, A. Two-year follow-up of amyloid deposition in patients with Alzheimer's disease. *Brain* **2006**, *129*, 2856–66.

(24) Choi, S. R.; Golding, G.; Zhuang, Z.; Zhang, W.; Lim, N.; Hefti, F.; Benedum, T. E.; Kilbourn, M. R.; Skovronsky, D.; Kung, H. F. Preclinical properties of 18F-AV-45: a PET agent for Abeta plaques in the brain. *J. Nucl. Med.* **2009**, *50*, 1887–94.

(25) Wong, D. F.; Rosenberg, P. B.; Zhou, Y.; Kumar, A.; Raymond, V.; Ravert, H. T.; Dannals, R. F.; Nandi, A.; Brasic, J. R.; Ye, W.; Hilton, J.; Lyketsos, C.; Kung, H. F.; Joshi, A. D.; Skovronsky, D. M.; Pontecorvo, M. J. In vivo imaging of amyloid deposition in Alzheimer disease using the radioligand 18F-AV-45 (florbetapir F18). *J. Nucl. Med.* **2010**, *51*, 913–20.

(26) Clark, C. M.; Schneider, J. A.; Bedell, B. J.; Beach, T. G.; Bilker, W. B.; Mintun, M. A.; Pontecorvo, M. J.; Hefti, F.; Carpenter, A. P.;

- Flitter, M. L.; Krautkramer, M. J.; Kung, H. F.; Coleman, R. E.; Doraiswamy, P. M.; Fleisher, A. S.; Sabbagh, M. N.; Sadowsky, C. H.; Reiman, E. P.; Zehntner, S. P.; Skovronsky, D. M.; Group, A. A. S. Use of florbetapir-PET for imaging beta-amyloid pathology. *J. Am. Med. Soc.* **2011**, *305*, 275–83.
- (27) Shokeen, M.; Anderson, C. J. Molecular Imaging of Cancer with Copper-64 Radiopharmaceuticals and Positron Emission Tomography (PET). *Acc. Chem. Res.* **2009**, *42*, 832–841.
- (28) Wadas, T. J.; Wong, E. H.; Weisman, G. R.; Anderson, C. J. Copper chelation chemistry and its role in copper radiopharmaceuticals. *Curr. Pharm. Des.* **2007**, *13*, 3–16.
- (29) Blower, P. J.; Lewis, J. S.; Zweit, J. Copper radionuclides and radiopharmaceuticals in nuclear medicine. *Nucl. Med. Biol.* **1996**, *23*, 957–980.
- (30) Maheshwari, V.; Dearling, J. L. J.; Treves, S. T.; Packard, A. B. Measurement of the rate of copper(II) exchange for  $^{64}\text{Cu}$  complexes of bifunctional chelators. *Inorg. Chim. Acta* **2012**, *393*, 318–323.
- (31) Voss, S. D.; Smith, S. V.; DiBartolo, N.; McIntosh, L. J.; Cyr, E. M.; Bonab, A. A.; Dearling, J. L. J.; Carter, E. A.; Fischman, A. J.; Treves, S. T.; Gillies, S. D.; Sargeson, A. M.; Huston, J. S.; Packard, A. B. Positron emission tomography (PET) imaging of neuroblastoma and melanoma with  $^{64}\text{Cu}$ -SarAr immunoconjugates. *Proc. Natl. Acad. Sci. U. S. A.* **2007**, *104*, 17489–17493.
- (32) Anderson, C. J.; Ferdani, R. Copper-64 radiopharmaceuticals for PET imaging of cancer: advances in preclinical and clinical research. *Cancer Biother. Radiopharm.* **2009**, *24*, 379–93.
- (33) Sun, X.; Wuest, M.; Weisman, G. R.; Wong, E. H.; Reed, D. P.; Boswell, C. A.; Motekaitis, R.; Martell, A. E.; Welch, M. J.; Anderson, C. J. Radiolabeling and In Vivo Behavior of Copper-64-Labeled Cross-Bridged Cyclam Ligands. *J. Med. Chem.* **2002**, *45*, 469–477.
- (34) Boswell, C. A.; Sun, X.; Niu, W.; Weisman, G. R.; Wong, E. H.; Rheingold, A. L.; Anderson, C. J. Comparative In Vivo Stability of Copper-64-Labeled Cross-Bridged and Conventional Tetraazamacrocyclic Complexes. *J. Med. Chem.* **2004**, *47*, 1465–1474.
- (35) Wong, E. H.; Weisman, G. R.; Hill, D. C.; Reed, D. P.; Rogers, M. E.; Condon, J. S.; Fagan, M. A.; Calabrese, J. C.; Lam, K.-C.; Guzei, I. A.; Rheingold, A. L. Synthesis and Characterization of Cross-Bridged Cyclams and Pendant-Armed Derivatives and Structural Studies of Their Copper(II) Complexes. *J. Am. Chem. Soc.* **2000**, *122*, 10561–10572.
- (36) Ferdani, R.; Stigers, D. J.; Fiamengo, A. L.; Wei, L.; Li, B. T. Y.; Golen, J. A.; Rheingold, A. L.; Weisman, G. R.; Wong, E. H.; Anderson, C. J. Synthesis, Cu(II) complexation,  $^{64}\text{Cu}$ -labeling and biological evaluation of cross-bridged cyclam chelators with phosphonate pendant arms. *Dalton Trans.* **2012**, *41*, 1938–1950.
- (37) Bartholomä, M. D. Recent developments in the design of bifunctional chelators for metal-based radiopharmaceuticals used in Positron Emission Tomography. *Inorg. Chim. Acta* **2012**, *389*, 36–51.
- (38) Ratnakar, S. J.; Viswanathan, S.; Kovacs, Z.; Jindal, A. K.; Green, K. N.; Sherry, A. D. Europium(III) DOTA-tetraamide Complexes as Redox-Active MRI Sensors. *J. Am. Chem. Soc.* **2012**, *134*, 5798–5800.
- (39) Rojas-Quijano, F. A.; Tircsó, G.; Tircsó, G.; Tircsó, G.; Baranyai, Z.; Tran Hoang, H.; Kálmán, F. K.; Gulaka, P. K.; Kodibagkar, V. D.; Aime, S.; Kovács, Z.; Sherry, A. D. Synthesis and Characterization of a Hypoxia-Sensitive MRI Probe. *Chem. - Eur. J.* **2012**, *18*, 9669–9676.
- (40) Green, K. N.; Viswanathan, S.; Rojas-Quijano, F. A.; Kovacs, Z.; Sherry, A. D. Europium(III) DOTA-Derivatives Having Ketone Donor Pendant Arms Display Dramatically Slower Water Exchange. *Inorg. Chem.* **2011**, *50*, 1648–1655.
- (41) Carney, C. E.; Tran, A. D.; Wang, J.; Schabel, M. C.; Sherry, A. D.; Woods, M. Towards the Rational Design of MRI Contrast Agents:  $\delta$ -Substitution of Lanthanide(III) NB-DOTA-Tetraamide Chelates Influences but Does Not Control Coordination Geometry. *Chem. - Eur. J.* **2011**, *17*, 10372–10378.
- (42) Varasteh, Z.; Velikyan, I.; Lindeberg, G.; Sörensen, J.; Larhed, M.; Sandström, M.; Selvaraju, R. K.; Malmberg, J.; Tolmachev, V.; Orlova, A. Synthesis and Characterization of a High-Affinity NOTA-Conjugated Bombesin Antagonist for GRPR-Targeted Tumor Imaging. *Bioconjugate Chem.* **2013**, *24*, 1144–1153.
- (43) Chang, A. J.; Sohn, R.; Lu, Z. H.; Arbeit, J. M.; Lapi, S. E. Detection of Rapalog-Mediated Therapeutic Response in Renal Cancer Xenografts Using  $^{64}\text{Cu}$ -bevacizumab ImmunoPET. *PLoS One* **2013**, *8*, 1–8.
- (44) Ferreira, C. L.; Bayly, S. R.; Green, D. E.; Storr, T.; Barta, C. A.; Steele, J.; Adam, M. J.; Orvig, C. Carbohydrate-appended 3-hydroxy-4-pyridinone complexes of the  $[\text{M}(\text{CO})(3)]^{+}$  core (M) Re, Tc-99m, Re-186). *Bioconjugate Chem.* **2006**, *17*, 1321–1329.
- (45) Ferreira, C. L.; Yapp, D. T. T.; Mandel, D.; Gill, R. K.; Boros, E.; Wong, M. Q.; Jurek, P.; Kiefer, G. E.  $^{68}\text{Ga}$  Small Peptide Imaging: Comparison of NOTA and PCTA. *Bioconjugate Chem.* **2012**, *23*, 2239–2246.
- (46) Bailey, G. A.; Price, E. W.; Zeglis, B. M.; Ferreira, C. L.; Boros, E.; Lacasse, M. J.; Patrick, B. O.; Lewis, J. S.; Adam, M. J.; Orvig, C. H2azapa: a Versatile Acyclic Multifunctional Chelator for  $^{67}\text{Ga}$ ,  $^{64}\text{Cu}$ ,  $^{111}\text{In}$ , and  $^{177}\text{Lu}$ . *Inorg. Chem.* **2012**, *51*, 12575–12589.
- (47) Boros, E.; Cawthray, J. F.; Ferreira, C. L.; Patrick, B. O.; Adam, M. J.; Orvig, C. Evaluation of the H2dedpa Scaffold and its cRGDyK Conjugates for Labeling with  $^{64}\text{Cu}$ . *Inorg. Chem.* **2012**, *51*, 6279–6284.
- (48) Esteves, C. V.; Lamosa, P.; Delgado, R.; Costa, J.; Désogère, P.; Rousselin, Y.; Goze, C.; Denat, F. Remarkable Inertness of Copper(II) Chelates of Cyclen-Based Macrobicycles with Two trans-N-Acetate Arms. *Inorg. Chem.* **2013**, *52*, 5138–5153.
- (49) Roger, M.; Lima, L. M. P.; Frindel, M.; Platas-Iglesias, C.; Gestin, J.-F.; Delgado, R.; Patinec, V.; Tripiet, R. Monopicolinate-dipicolyl Derivative of Triazacyclononane for Stable Complexation of  $\text{Cu}^{2+}$  and  $^{64}\text{Cu}^{2+}$ . *Inorg. Chem.* **2013**, *52*, 5246–5259.
- (50) Comba, P.; Hunoldt, S.; Morgen, M.; Pietzsch, J.; Stephan, H.; Wadepohl, H. Optimization of Pentadentate Bispindines as Bifunctional Chelators for  $^{64}\text{Cu}$  Positron Emission Tomography (PET). *Inorg. Chem.* **2013**, *52*, 8131–8143.
- (51) Sharma, A. K.; Pavlova, S. T.; Kim, J.; Finkelstein, D.; Hawco, N. J.; Rath, N. P.; Kim, J.; Mirica, L. M. Bifunctional Compounds for Controlling Metal-Mediated Aggregation of the  $\text{A}\beta$ 42 Peptide. *J. Am. Chem. Soc.* **2012**, *134*, 6625–6636.
- (52) Sharma, A. K.; Kim, J.; Prior, J. T.; Hawco, N. J.; Rath, N. P.; Kim, J.; Mirica, L. M. Small Bifunctional Chelators That Do Not Disaggregate Amyloid  $\beta$  Fibrils Exhibit Reduced Cellular Toxicity. *Inorg. Chem.* **2014**, *53*, 11367–11376.
- (53) Sharma, A. K.; Pavlova, S. T.; Kim, J.; Mirica, L. M. The effect of  $\text{Cu}^{2+}$  and  $\text{Zn}^{2+}$  on the  $\text{A}\beta$ [small beta]42 peptide aggregation and cellular toxicity. *Metallomics* **2013**, *5*, 1529–1536.
- (54) Zhang, Y.; Rempel, D. L.; Zhang, J.; Sharma, A. K.; Mirica, L. M.; Gross, M. L. Pulsed hydrogen–deuterium exchange mass spectrometry probes conformational changes in amyloid beta ( $\text{A}\beta$ ) peptide aggregation. *Proc. Natl. Acad. Sci. U. S. A.* **2013**, *110*, 14604–14609.
- (55) Necula, M.; Kaye, R.; Milton, S.; Glabe, C. G. Small Molecule Inhibitors of Aggregation Indicate That Amyloid  $\beta$  Oligomerization and Fibrillization Pathways Are Independent and Distinct. *J. Biol. Chem.* **2007**, *282*, 10311–10324.
- (56) Kim, W. D.; Hrcir, D. C.; Kiefer, G. E.; Sherry, A. D. Synthesis, Crystal Structure, and Potentiometry of Pyridine-Containing Tetraaza Macrocyclic Ligands with Acetate Pendant Arms. *Inorg. Chem.* **1995**, *34*, 2225–2232.
- (57) Kim, W. D.; Kiefer, G. E.; Maton, F.; McMillan, K.; Muller, R. N.; Sherry, A. D. Relaxometry, Luminescence Measurement, Electrophoresis, and Animal Biodistribution of Lanthanide(III) Complexes of Some Polyaza Macrocyclic Acetates Containing Pyridine. *Inorg. Chem.* **1995**, *34*, 2233–2243.
- (58) Bottino, F.; Di Grazia, M.; Finocchiaro, P.; Fronczek, F. R.; Mamo, A.; Pappalardo, S. Reaction of Tosylamide Monosodium Salt with Bis(halomethyl) Compounds: an Easy Entry to Symmetrical N-tosylazamacrocycles. *J. Org. Chem.* **1988**, *53*, 3521–9.
- (59) Wessel, A. J.; Schultz, J. W.; Tang, F.; Duan, H.; Mirica, L. M. Improved Synthesis of Symmetrically & Asymmetrically N-Substituted Pyridinophane Derivatives. *Org. Biomol. Chem.* **2017**, submitted.

- (60) Koek, J. H.; Russell, S. W.; vanderWolf, L.; Hage, R.; Warnaar, J. B.; Spek, A. L.; Kerschner, J.; DelPizzo, L. Improved syntheses, structures, spectral and electrochemical properties of  $[\text{Mn-2(III)}(\mu\text{-O})(\mu\text{-O}(2)\text{CMe})(2)\text{L}(2)](2+)$  and  $[\text{Mn-2(IV)}(\mu\text{-O})(3)\text{L}(2)](2+)$  complexes. Two homologous series derived from eight N-substituted 1,4,7-triazacyclononanes. *J. Chem. Soc., Dalton Trans.* **1996**, 353–362.
- (61) Mirica, L. M.; Sharma, A. K.; Schultz, J. W. Metal-Binding Bifunctional Compounds as Diagnostic Agents for Alzheimer's Disease. U.S. Patent 2015/0209452, July 30, 2015.
- (62) Sheldrick, G. M. Bruker-SHELXTL. *Acta Crystallogr., Sect. A: Found. Crystallogr.* **2008**, *64*, 112–122.
- (63) See the [Supporting Information](#).
- (64) Gans, P.; Sabatini, A.; Vacca, A. Determination of equilibrium constants from spectrophotometric data obtained from solutions of known pH: The program pHab. *Ann. Chim.* **1999**, *45*.
- (65) Alderighi, L. Hyperquad simulation and speciation (HySS): A utility program for the investigation of equilibria involving soluble and partially soluble species. *Coord. Chem. Rev.* **1999**, *184*, 311.
- (66) Sharma, A. K.; Kim, J.; Prior, J. T.; Hawco, N. J.; Rath, N. P.; Kim, J.; Mirica, L. M. Small Bifunctional Chelators that Do Not Dissagregate Amyloid Fibrils Show Reduced Cellular Toxicity. *Inorg. Chem.* **2014**, *53*, 11367–11376.
- (67) Storr, T.; Merkel, M.; Song-Zhao, G. X.; Scott, L. E.; Green, D. E.; Bowen, M. L.; Thompson, K. H.; Patrick, B. O.; Schugar, H. J.; Orvig, C. Synthesis, characterization, and metal coordinating ability of multifunctional carbohydrate-containing compounds for Alzheimer's therapy. *J. Am. Chem. Soc.* **2007**, *129*, 7453–7463.
- (68) Hickey, J. L.; Lim, S.; Hayne, D. J.; Paterson, B. M.; White, J. M.; Villemagne, V. L.; Roselt, P.; Binns, D.; Cullinane, C.; Jeffery, C. M.; Price, R. I.; Barnham, K. J.; Donnelly, P. S. Diagnostic Imaging Agents for Alzheimer's Disease: Copper Radiopharmaceuticals that Target A beta Plaques. *J. Am. Chem. Soc.* **2013**, *135*, 16120–16132.
- (69) Martell, A. E.; Smith, R. M. *Critical Stability Constants*; Plenum: New York, 1976; Vol. IV, p 1.
- (70) Bandara, N.; Sharma, A. K.; Krieger, S.; Schultz, J. W.; Han, B. H.; Rogers, B. E.; Mirica, L. M. Evaluation of  $^{64}\text{Cu}$ -Based Radiopharmaceuticals that Target A $\beta$  Peptide Aggregates as Diagnostic Tools for Alzheimer's Disease. *J. Am. Chem. Soc.* **2017**, *139*, 12550–12558.
- (71) Khusnutdinova, J. R.; Luo, J.; Rath, N. P.; Mirica, L. M. Late First-Row Transition Metal Complexes of a Tetradentate Pyridinophane Ligand: Electronic Properties and Reactivity Implications. *Inorg. Chem.* **2013**, *52*, 3920–3932.
- (72) Chaudhuri, P.; Querbach, J.; Wieghardt, K.; Nuber, B.; Weiss, J. Synthesis, electrochemistry, and magnetic properties of binuclear cobalt complexes containing the  $\text{Co}_2(\mu\text{-x})(\mu\text{-carboxylato})_2\text{n}+$  core ( $x = \text{oh, cl, or br - n} = 1-3$ ) - the crystal structures of  $[\text{Co}_2\text{ii}(\mu\text{-chl}_2\text{cco}_2)_2(\mu\text{-cl})_2]\text{pf}_6$  and  $[\text{Co}_2\text{iii}(\mu\text{-meco}_2)_2(\mu\text{-oh})_2][\text{clo}_4]_2 \cdot 0.5\text{h}_2\text{o}$  ( $l = n, n', n''$ -trimethyl-1,4,7-triazacyclononane). *J. Chem. Soc., Dalton Trans.* **1990**, 271–278.
- (73) Mukherjee, A.; Lloret, F.; Mukherjee, R. Synthesis and Properties of Diphenoxo-Bridged CoII, NiII, CuII, and ZnII Complexes of a New Tripodal Ligand: Generation and Properties of MII-Coordinated Phenoxyl Radical Species. *Inorg. Chem.* **2008**, *47*, 4471–4480.
- (74) Garribba, E.; Micera, G. The determination of the geometry of Cu(II) complexes - An EPR spectroscopy experiment. *J. Chem. Educ.* **2006**, *83*, 1229–1232.
- (75) Halcrow, M. A. Interpreting and controlling the structures of six-coordinate copper(II) centres - when is a compression really a compression? *Dalton Trans.* **2003**, 4375–4384.
- (76) Hathaway, B. J.; Billing, D. E. The electronic properties and stereochemistry of mono-nuclear complexes of the copper(II) ion. *Coord. Chem. Rev.* **1970**, *5*, 143–207.
- (77) Hathaway, B. J.; Tomlinson, A. A. G. Copper(II) ammonia complexes. *Coord. Chem. Rev.* **1970**, *5*, 1–43.
- (78) Lever, A. B. P. *Inorganic electronic spectroscopy*; Elsevier, 1984.
- (79) Woodin, K. S.; Heroux, K. J.; Boswell, C. A.; Wong, E. H.; Weisman, G. R.; Niu, W.; Tomellini, S. A.; Anderson, C. J.; Zakharov, L. N.; Rheingold, A. L. Kinetic Inertness and Electrochemical Behavior of Copper(II) Tetraazamacrocyclic Complexes: Possible Implications for in Vivo Stability. *Eur. J. Inorg. Chem.* **2005**, *2005*, 4829–4833.
- (80) Gong, Y. S.; Chang, L.; Viola, K. L.; Lacor, P. N.; Lambert, M. P.; Finch, C. E.; Krafft, G. A.; Klein, W. L. Alzheimer's disease-affected brain: Presence of oligomeric A beta ligands (ADDLs) suggests a molecular basis for reversible memory loss. *Proc. Natl. Acad. Sci. U. S. A.* **2003**, *100*, 10417–10422.
- (81) Walsh, D. M.; Selkoe, D. J. A beta Oligomers - a decade of discovery. *J. Neurochem.* **2007**, *101*, 1172–1184.
- (82) Haass, C.; Selkoe, D. J. Soluble protein oligomers in neurodegeneration: lessons from the Alzheimer's amyloid beta-peptide. *Nat. Rev. Mol. Cell Biol.* **2007**, *8*, 101–112.
- (83) Eiblmaier, M.; Andrews, R.; Laforest, R.; Rogers, B. E.; Anderson, C. J. Nuclear uptake and dosimetry of Cu-64-labeled chelator-somatostatin conjugates in an SSTr2-transfected human tumor cell line. *J. Nucl. Med.* **2007**, *48*, 1390–1396.
- (84) Braymer, J. J.; DeToma, A. S.; Choi, J.-S.; Ko, K. S.; Lim, M. H. Recent Development of Bifunctional Small Molecules to Study Metal-Amyloid- $\beta$  Species in Alzheimer's Disease. *Int. J. Alzheimer's Dis.* **2011**, *2011*, 623051.
- (85) Choi, J.-S.; Braymer, J. J.; Nanga, R. P. R.; Ramamoorthy, A.; Lim, M. H. Design of small molecules that target metal-A $\beta$  species and regulate metal-induced A $\beta$  aggregation and neurotoxicity. *Proc. Natl. Acad. Sci. U. S. A.* **2010**, *107*, 21990–21995.